

AD-A142 095

(12)

DIAGNOSTICS DEVELOPMENT FOR E-BEAM EXCITED AIR CHANNELS

Technical Report No. 4

OPTICAL STUDIES OF THE PHERMEX ELECTRON BEAM

March 20, 1984

By: D.J. Eckstrom and J.S. Dickinson

Sponsored by:

DEFENSE ADVANCED RESEARCH PROJECTS AGENCY
1400 Wilson Blvd.
Arlington, VA 22209

Monitored by:

OFFICE OF NAVAL RESEARCH
800 North Quincy Street
Arlington, VA 22217

ARPA Order No. 4128
Contract No. N00014-81-C-0208
Effective Date: 15 January 1981
Expiration Date: 31 May 1984
Principal Investigator: D.J. Eckstrom (415) 859-4398

SRI Project PYU 2690
MP Report No. 84-055

The views and conclusions contained in this document are those of the authors and should not be interpreted as necessarily representing official policies, either expressed or implied, of the Defense Advanced Research Projects Agency or the U.S. Government.

SRI International
333 Ravenswood Avenue
Menlo Park, California 94025
(415) 326-6200
TWX: 910-373-2046
Telex: 334 486

This document has been approved
for public release and sale; its
distribution is unlimited.

84 06 14 021

FILE COPY



UNCLASSIFIED

SECURITY CLASSIFICATION OF THIS PAGE (When Data Entered)

REPORT DOCUMENTATION PAGE		READ INSTRUCTIONS BEFORE COMPLETING FORM
1. REPORT NUMBER	2. GOVT ACCESSION NO.	3. RECIPIENT'S CATALOG NUMBER
AD-A143095		
4. TITLE (and Subtitle) DIAGNOSTICS DEVELOPMENT FOR E-BEAM EXCITED AIR CHANNELS. Optical Studies of the PHERMEX Electron Beam		5. TYPE OF REPORT & PERIOD COVERED Technical Report No. 4
		6. PERFORMING ORG. REPORT NUMBER MP Report No. 84-055
7. AUTHOR(s) D. J. Eckstrom and J. S. Dickinson		8. CONTRACT OR GRANT NUMBER(s) N00014-81-C-0208
9. PERFORMING ORGANIZATION NAME AND ADDRESS SRI International 333 Ravenswood Ave. Menlo Park, CA 94025		10. PROGRAM ELEMENT PROJECT TASK AREA & WORK UNIT NUMBERS ARPA Order No. 4128
11. CONTROLLING OFFICE NAME AND ADDRESS Defense Advanced Research Projects Agency 1400 Wilson Boulevard Arlington, VA 22209		12. REPORT DATE March 20, 1984
		13. NUMBER OF PAGES 73
14. MONITORING AGENCY NAME & ADDRESS (if different from Controlling Office) Office of Naval Research 800 North Quincy Street Arlington, VA 22217		15. SECURITY CLASS (of this report) Unclassified
		15a. DECLASSIFICATION DOWNGRADING SCHEDULE N/A
16. DISTRIBUTION STATEMENT (of this Report) Approved for public release; distribution unlimited.		
17. DISTRIBUTION STATEMENT (of the abstract entered in Block 20, if different from Report)		
18. SUPPLEMENTARY NOTES		
19. KEY WORDS (Continue on reverse side if necessary and identify by block number) Charged particle beams, optical radiation, air fluorescence, optical thermometry, optical Faraday cup.		
20. ABSTRACT (Continue on reverse side if necessary and identify by block number) Electron-induced fluorescence at selected uv wavelengths from the air channel excited by the PHERMEX electron beam facility at LANL was studied. Each beam pulse consisted of a sequence of 10 micropulses of 26 meV electrons of 200 A peak current lasting 3 ns. Individual micropulses were measured and analyzed. (continued on back page)		

UNCLASSIFIED

SECURITY CLASSIFICATION OF THIS PAGE(When Data Entered)

20. Abstract (continued)

The results of this study can be summarized as follows:

- a) → The 391.4-nm first negative emission from N_2^+ was linear with beam current for all micropulses at all pressures. Thus, this emission band serves as an optical Faraday cup under these conditions.
- b) → The 406.0-nm N_2 second positive emission exhibited enhancements due to self-induced electric fields at pressures below 50 torr.
- c) → The vibrational temperatures in the air channel rose during each pulse train to values ranging from about 750 to 1400 K.
- d) → Very limited data indicates that the rotational temperature stays constant at ^{approx.} 300 K.
- e) → Emission measurements made 20-m off the beam axis indicate that the induced intensity decays rapidly with propagation distance (30-50% in 6 meters). This suggests a much faster dissipation of beam energy than suggested by energy deposition calculations.
- f) → We observed no evidence for super radiant emission during tests at 580 torr.

UNCLASSIFIED

SECURITY CLASSIFICATION OF THIS PAGE(When Data Entered)

ACKNOWLEDGMENTS

This measurement program was greatly facilitated by the assistance of the staff at the PHERMEX facility at Los Alamos National Laboratory, including T. P. Starke, D. C. Moir, L. A. Buita, E. W. Pogue, and J. S. Sandoval. We are also indebted to R. R. Karl and M. I. Buchwald of the Atmospheric Sciences Group at LANL for both equipment support and useful technical discussions.



ACCOMPLISHED FOR
RECEIVED
DATE
BY

H-1

CONTENTS

ACKNOWLEDGMENTS.....	1
LIST OF FIGURES.....	111
I INTRODUCTION.....	1
II EXPERIMENTAL TECHNIQUES.....	3
Background.....	3
Instrumentation.....	4
Calibration.....	6
Predicted Absolute Intensities.....	8
III RESULTS.....	10
Absolute 391.4-nm Emission.....	10
Absolute 406.0-nm Emission.....	11
Vibrational Temperatures.....	12
Rotational Temperatures.....	13
Far-Field Emission Measurements.....	13
Search for Superradiant Emission.....	14
IV CONCLUSIONS.....	16
REFERENCES.....	18

FIGURES

1. Electronic States of N_2 and N_2^+ Relevant to Optical Beam Diagnostics
2. Optical Layout for Temperature Measurements (Mod 2)
3. Setup for Optical Measurements at PHERMEX
4. Typical Intensity Histories for PHERMEX Exciting Air at 580 torr
5. Setup for Far-Field Optical Measurements and Rotational Temperature Determinations
6. Normalized 391.4-nm Signals versus Micropulse at 580 torr
7. Normalized 391.4-nm Signals versus Micropulse at 300 torr
8. Normalized 391.4-nm Signals versus Micropulse at 100 torr
9. Normalized 391.4-nm Signals versus Micropulse at 50 torr
10. Normalized 391.4-nm Signals versus Micropulse at 30 torr
11. Normalized 391.4-nm Signals versus Micropulse at 10 torr
12. Normalized 392.4-nm Signals versus Micropulse at 5 torr
13. Normalized 391.4-nm Signals versus Pressure for Micropulse No. 1
14. Normalized 391.4-nm Signals versus Pressure for Micropulse No. 2
15. Normalized 391.4-nm Signals versus Pressure for Micropulse No. 3
16. Normalized 391.4-nm Signals versus Pressure for Micropulse No. 4
17. Normalized 391.4-nm Signals versus Pressure for Micropulse No. 5
18. Normalized 391.4-nm Signals versus Pressure for Micropulse No. 6
19. Normalized 391.4-nm Signals versus Pressure for Micropulse No. 7
20. Normalized 391.4-nm Signals versus Pressure for Micropulse No. 8
21. Normalized 391.4-nm Signals versus Pressure for Micropulse No. 9
22. Superposition of all Normalized 391.4-nm Signals versus Pressure
23. Normalized 406.0-nm Signals versus Micropulse at 580 torr
24. Normalized 406.0-nm Signals versus Micropulse at 300 torr
25. Normalized 406.0-nm Signals versus Micropulse at 100 torr
26. Normalized 406.0-nm Signals versus Micropulse at 50 torr
27. Normalized 406.0-nm Signals versus Micropulse at 30 torr
28. Normalized 406.0-nm Signals versus Micropulse at 10 torr
29. Normalized 406.0-nm Signals versus Micropulse at 5 torr
30. Normalized 406.0-nm Signals versus Pressure for Micropulse No. 1
31. Normalized 406.0-nm Signals versus Pressure for Micropulse No. 2

32. Normalized 406.0-nm Signals versus Pressure for Micropulse No. 3
33. Normalized 406.0-nm Signals versus Pressure for Micropulse No. 4
34. Normalized 406.0-nm Signals versus Pressure for Micropulse No. 5
35. Normalized 406.0-nm Signals versus Pressure for Micropulse No. 6
36. Normalized 406.0-nm Signals versus Pressure for Micropulse No. 7
37. Normalized 406.0-nm Signals versus Pressure for Micropulse No. 8
38. Normalized 406.0-nm Signals versus Pressure for Micropulse No. 9

39. Superposition of all 406.0-nm Signals versus Pressure

40. Ratio of 391.4 nm/423.6-nm Signals versus Micropulse at 580 torr
41. Ratio of 391.4 nm/423.6-nm Signals versus Micropulse at 300 torr
42. Ratio of 391.4 nm/423.6-nm Signals versus Micropulse at 100 torr
43. Ratio of 391.4 nm/423.6-nm Signals versus Micropulse at 50 torr
44. Ratio of 391.4 nm/423.6-nm Signals versus Micropulse at 30 torr
45. Ratio of 391.4 nm/423.6-nm Signals versus Micropulse at 10 torr
46. Ratio of 391.4 nm/423.6-nm Signals versus Micropulse at 5 torr

47. Ratio of 406.0 nm/403.0-nm Signals versus Micropulse at 580 torr

48. Far-Field Intensity Histories for PHERMEX Beam Propagating in Open Air

I INTRODUCTION

As part of our research program to develop and apply optical diagnostics for high energy electron beams propagating in air, we participated in the Project Banda test series at the PHERMEX facility at Los Alamos National Laboratory (LANL) from 17 to 27 August 1983. Our primary interest was in performing optical measurements of vibrational and rotational temperatures (T_V and T_R , respectively) on an electron beam that produced repetitive, closely spaced pulses and that, under ideal conditions, could have produced substantial channel heating. Our second goal was to test the optical Faraday cup (light intensity proportional to beam current) under these beam conditions. A third goal was to explore the use of far-field optical emission measurements in monitoring beam propagation characteristics. Finally, a minor effort was made to search for superradiant emission along the beam axis.

The PHERMEX facility has been described by Starke [St83]. Additional descriptions of the machine performance and operating parameters for the Project Banda tests are given in [SD83, BMP83]. Briefly, PHERMEX is an rf-driven linear accelerator that operates in a burst-pulse mode. The total pulse envelope is approximately 200 ns long and contains 9 to 12 individual pulses ("micropulses") of 3 ns FWHM spaced by 20 ns. For the tests reported here, the beam energy was ~ 26 MeV and the peak current (micropulses 3-6) was approximately 200 A. The beam diameter at the exit foil was approximately 1 mm, but the beam diverged to about 3-4 mm diameter at our observation zone which extended from 7 to 17 cm downstream.

The air channel heating produced by the PHERMEX beam can be estimated by assuming that the stopping power of a 25-MeV electron beam in air is 2.4 kV/cm-atmagat [HB56] or 1.8 kV/cm at the 580 torr pressure of Los Alamos. (This is the contribution due to direct primary beam excitation only. "Ohmic heating" caused by acceleration of plasma electrons by the self-induced electric field would be in addition to the values given here.) The total charge in the pulse ($\int Idt$) was $\sim 5 \mu C$ (average current of 150 A for 12 micropulses of 3-ns duration each). Thus, the energy deposition was

$\sim 9 \times 10^{-3}$ J/cm. For a beam diameter of 3 mm, the volumetric energy density was then ~ 0.13 J/cm³.

If we assume that this energy is fully equilibrated in the air channel, we can calculate the temperature rise, based on a specific heat of 7 cal/mol K (29.3 J/mol K) and a density of 3.4×10^{-5} mol/cm³, to be 130 K. However, much of this energy is deposited as ionization or electronic state excitation, and the equilibration probably occurs as a cascade of energy through the $N_2(A^3\Sigma)$ state to the vibrational levels (N_2^+) of the $N_2(X)$ ground state. The quenching time of the A-state is about 65 ns in 580 torr of air, whereas the relaxation time for N_2^+ in air ranges from 0.1 to 100 ms, depending on the relative humidity of the air. Thus, we might expect energy cascade to N_2^+ during the pulse, but very little relaxation to the translational/rotational degrees of freedom.

If we assume that all the beam-deposited energy goes into vibrational excitation, we can calculate the resulting vibrational temperature from the relation

$$e_v = \frac{R\theta_v}{\exp(\theta_v/T_v) - 1}$$

where $\theta_v = 3390$ K for N_2 . For $e_v = 0.13$ J/cm³, this gives $\Delta T_v \approx 1580$ K or $T_v = 1880$ K.

Two additional points are worth noting. First, under conditions where the beam propagates with a 1 mm diameter, the channel heating would be proportionately larger ($\sim 10\times$) than the values given above and thus would offer the opportunity of diagnostics studies in a regime not yet investigated. Second, plasma excitation effects ("ohmic heating") will become more important at lower pressures and must be considered in addition to the direct beam excitation considered above. The normalized field strength, E/p (or E/N), where E is the self-induced axial field in the beam, will increase with decreasing p , and so the accelerated plasma electrons will cause additional excitation of vibrational, electronic, and finally ionization modes. We interpret our results to include both vibrational and electronic excitation effects as discussed in Section III.

II EXPERIMENTAL TECHNIQUE

Background

The optical emission from air excited by low current, high energy electron beams has been studied at both low and high (~ 1 atm) pressures [cf. DO64, BD67, Ha68, OD69, Mi70, HPE70, La73]. These studies together with theoretical predictions of excitation rates [KK73, KK79] and excited state quenching rates have established fluorescence efficiencies (η_F = power radiated/power deposited) for a large number of transitions, primarily in N_2 and N_2^+ . Insofar as these fluorescence efficiencies remain constant under conditions of high electron beam current and various beam geometries, the intensity of a selected optical transition is proportional to beam current, giving rise to the "optical Faraday cup" [H180].

The principal emission band systems in atmospheric pressure air are the $N_2^+(B^2\Sigma \rightarrow X^2\Sigma)$ first negative and the $N_2(C^3\Pi-B^3\Pi)$ second positive systems. We have chosen the 391.4-nm band ($v'=0 \rightarrow v''=0$) of the first negative system as the best candidate for an optical Faraday cup. This transition is preferable to a second positive band because (a) the upper state, $N_2^+(B)$, has a higher energy than $N_2(C)$ and thus is less susceptible to secondary excitation processes, (b) the excitation occurs over a broader range of electron energies and thus responds directly to excitation by beam cascade electrons, and (c) the quenching rate in air is higher so that the temporal response to beam current variations is faster.

Electron-beam-induced fluorescence also offers the possibility of determining the vibrational and rotational temperature of the air. This has been recognized and exploited for very low pressure air for some time [LW69, SHS70, SH71, OPH74, KH74]; application of the technique to atmospheric pressure air was proposed by Hill in 1980 [H180]. The principle of the vibrational temperature monitor is shown in Figure 1. Because the $N_2(X)$ ground state and the $N_2^+(B)$ state have nearly identical internuclear separation and similar vibrational spacing, it is assumed that electron beam excitation obeys optical Franck-Condon selection rules. Thus, $N_2(X, v''=0)$ is

excited primarily to $N_2^+(B, v'=0)$, and $N_2(X, v''=1)$ is excited primarily to $N_2^+(B, v'=1)$. We therefore measure the intensity of the $N_2^+(B, v'=0 \rightarrow X, v''=0)$ band at 391.4 nm and the $N_2^+(B, v'=1 \rightarrow X, v''=2)$ band at 423.6 nm to determine the ratio of populations of $N_2(X, v=0)$ and $N_2(X, v=1)$, and from that ratio determine the vibrational temperature, T_v , of N_2 .

The rotational temperature is determined by measuring the intensity distribution within a single vibronic band of N_2 or N_2^+ . This reflects the rotational population distribution and, insofar as equilibrium is maintained, yields the rotational temperature, T_R , which we also assume is the same as the translational or gas temperature. For convenience, we study the $N_2(C, v'=0 \rightarrow B, v''=3)$ second positive band at 406.0 nm; this transition was chosen as a compromise between fluorescence yield and transmission of the fiber optic in our detection system. We use two optical filters to isolate a spectral region near the band head (406.0 nm) and a second region in the blue wing of the band (403.0 nm).

Instrumentation

Our optical detection system is shown schematically in Figures 2 and 3. The primary feature of the design is a bundle of four 600- μ m quartz optical fibers (Quartz Products Corporation QSF-A-600) that transport the radiation from the beam channel (centered 12 cm downstream from the foil, with a 10-cm field of view, as shown in Figure 3) to a detector box containing collimating lenses, optical filters, and two Hamamatsu R1294U double microchannel plate photomultipliers (response time ~ 0.25 ns). Two of the fibers are 33.5 m long, whereas the other two are 55.5 m long. In normal operation, the 391.4- and 423.6-nm signals that are used to determine T_v are recorded first on the two photomultipliers, and the 406.0- and 403.0-nm signals used to determine T_R are delayed by 100 ns in the longer fibers and are subsequently "multiplexed" onto the same two photomultipliers. In the present tests, which involved 9 to 12 micropulses over a period of ~ 200 ns, no attempt was made to multiplex the signals, but rather shutters within the detector box were used to block pairs of signals in turn, so that only one of the temperatures could be measured on any single shot. The signals from the photomultipliers were recorded on two Tektronix 7104 oscilloscopes that were kindly loaned to us by the LANL staff. Typical intensity histories for $p = 580$ torr are shown in Figure 4;

as just noted, the 391.4- and 423.6-nm signals are from one shot, and the 406.0- and 403.0-nm signals are from a different shot.

The detector box was located in the steel bunker labeled R-290, which is located approximately 10 m downstream and 10 m to the right (south) of the beam exit. Past experience with this optical system at the Experimental Test Accelerator facility at Lawrence Livermore National Laboratory indicated that x-rays (or electrons produced in air by the x-rays) induced interfering optical signals in the fibers and that these background signals could be substantially reduced by encasing the fibers in thin-walled metal tubing. We use a double shield consisting of 1/4-inch copper tubing within 1/2-inch aluminum flexible electrical conduit. However, this was not adequate in the PHERMEX environment, and we were forced to run the cable along the ground from the firing point to the bunker and to shield it with a layer of lead bricks and one or more layers of 1/8-inch sheet lead. The channel emission and x-ray-induced fiber emission were readily compared by closing the remotely operated shutter located at the observation window on the propagation tank.

An even more serious problem existed in the bunker, where it was necessary to encase the detector box in a lead housing with walls 4 inches thick. Even after these efforts, x-ray signals in the photomultipliers and/or optical fibers caused a serious degradation of the signal-to-noise levels of the data.

On the fourth day of experiments, the windows were removed from the propagation tank and the collimator was removed. We then realigned the pickup head to observe a region near the beam exit foil (approximately 2 to 12 cm downstream) in the hope that the beam would be smaller in diameter so that channel temperatures would be higher. This obviously restricted measurements to local atmospheric pressure. We did not detect any significant differences from the previous measurements, and the results are reported together. The total number of shots at each condition was as follows:

<u>Pressure (torr)</u>	<u>T_V (391.4/423.6 nm)</u>	<u>T_R (406.0/403.0 nm)</u>
580	10	16
300	2	2
100	2	2
50	6	5
30	3	1
10	2	2
5	3	0
0.5	1	3
0.05	1	1

Our "far-field" optical measurements did not use the optical fiber system. Rather, a photomultiplier was enclosed in a lead housing located 21 m to the right and 3 m downstream of the exit foil, as shown in Figure 5. A turning mirror was used to provide an optical view of the beam path while blocking the direct x-ray line of sight. The mirror and PMT were aligned by looking back from the beam line at the center of the field of view (approximately 3.5 m downstream from the exit foil) and ensuring that the face of the PMT was centered on the viewer. In comparing results of these tests with those of other experimenters, it should be kept in mind that we were not able to perform calibrations to ensure that the detector response was uniform over the entire 7-m field of view. However, we have no reason to believe that was not the case.

Calibration

Two types of calibrations are relevant to this test program. The first concerns the absolute response of the detector system, i.e., the voltage response of each PMT for a given intensity level at the beam channel. The second is the ratio of the signal levels for the 391.4/423.6-nm channels as a function of T_V and for the 406.0/403.0-nm channels as a function of T_R.

Hamamatsu microchannel plate photomultipliers present a difficulty for calibration because they have a built-in 50-ohm load resistor. Standard cw calibration procedures using a standard lamp cannot be used because the tube saturates for cw light levels that are too low to permit an accurate photo-current measurement. Because we did not have a calibrated pulsed light source

available, we base our calibration for absolute response on the manufacturer's gain and quantum efficiency versus wavelength curves furnished with the tubes. For the transmission of the fibers, we use an attenuation coefficient as a function of wavelength that is an average between our measurements and the vendor's specifications (the uncertainty in transmission is about $\pm 25\%$). We have measured the transmission of each optical filter as a function of wavelength and have convolved that transmission with the calculated spectral intensity versus wavelength of the relevant band to calculate the effective transmission of the filter. The field of view and the fiber collection solid angles were based on the geometry and numerical aperture of the fibers. The net transmission of the tank window and of the collimating lens was assumed to be 80%. The product of these factors gives a response of 170 mV/(W/cm) at 391.4 nm and 66 mV/(W/cm) at 406.0 nm when each PMT gain was 1×10^6 .

Our calibrations to date of the signal ratios for the two pairs of intensity channels as a function of T_V and T_R are based on measurements we made of emission from shock-heated air excited by a Febetron 706 (600 keV, 5000 A, 3-ns pulse with a 2 cm diameter). The electron beam passes through a foil mounted in a hibachi structure in the end wall of a 5-cm ID shock tube; the beam is fired approximately 500 μ s after the reflected shock wave passes the observation window moving back upstream. In this way we measured temperatures in the range of 1000 to 3000 K; the resulting signal ratios are extrapolated smoothly to values obtained in open air at 300 K to provide the calibration curves used in analyzing the present data.

There are several uncertainties in these curves. First, we have not independently verified that the shock-heated air had reached full vibrational equilibrium at the time of the e-beam firing although we assign each measured signal ratio to the calculated equilibrium temperature for that shock strength. Second, the measured signal ratio for the 391.4/423.6-nm bands (used to determine T_V) should be a function of T_R because the convolutions of the spectral intensity distributions with the optical filter transmissions change. Thus, shock tube measurements where $T_R = T_V$ should not give the same signal ratio as beam experiments where T_V may be high while T_R remains near 300 K, even when T_V is the same in both experiments. Calculations show that a given signal ratio corresponds to a higher T_V when $T_R < T_V$ than when the two

temperatures are equal, with the effect becoming more pronounced as the temperature difference increases. However, because we have not yet reproduced the calculated signal ratio for $T = 300$ K, we will use the shock-tube results without correction, bearing in mind that the resulting values of T_V are a lower limit to the actual values. (Note that this uncertainty does not enter the calibration curves for T_R .)

A final uncertainty in the calibrations concerns nonlinearities in the intensities of various spectral bands with beam current. We have thus far assumed that results obtained with the Febetron 706 are free of these nonlinearities (such as self-induced-field plasma excitation effects), but we have not verified this assumption, and it is possible that both the differences between calculated and measured signal ratios and the scatter that we observe in calibration tests could be due to these effects.

In conclusion, we believe that the vibrational temperatures deduced from our measurements in these tests are lower limits to the correct values, and that the rotational temperatures are accurately calibrated. The absolute intensities of the N_2 and N_2^+ emission bands determined from our measurements could have some uncertainty because we have not performed a single-step absolute calibration of our system response.

Predicted Absolute Intensities

We will be comparing our absolute intensity measurements with expected values based on previously measured values of energy deposition in air, of fluorescence efficiencies for the first negative bands of N_2^+ and the second positive bands of N_2 , and of the quenching rates of these bands in air. The calculation of these predicted intensities are presented here.

The collisional energy loss of 25-MeV electrons in air is 3.4×10^{-6} ergs cm^2/g [HB56], which is equivalent to 2.4 keV/cm-amagat. (This is slightly higher than the canonical value of 2 keV/cm-amagat, which is approximately correct from 0.1 to 10 MeV.) At the LANL standard atmospheric pressure of 580 torr (0.76 amagat), the collisional energy deposition is therefore 3.1×10^{-9} ergs/cm or 1.8 keV/cm.

The fluorescence yield for the 391.4-nm band in air at low pressure is $\eta_{F_0} = 4.8 \times 10^{-3}$ [HPE70]. The two-body quenching rates of the $N_2^+(B, v=0)$

state by N_2 and O_2 are $(4.5 \pm 0.4) \times 10^{-10} \text{ cm}^3/\text{s}$ and $(7.5 \pm 1.0) \times 10^{-10} \text{ cm}^3/\text{s}$, respectively [Mi70, HPE70, BD67, CS71, MM71, TWF72]; in addition, Mitchell [Mi70] reports a three-body quenching by O_2 , with either N_2 or O_2 as the third body, with a rate of $3.1 \times 10^{-29} \text{ cm}^6/\text{s}$. The radiative decay rate is $A = 1.6 \times 10^7 \text{ s}^{-1}$ [RD78]. At finite pressures, the fluorescence yield is given by the relation

$$\eta_F = \eta_{F_0} A / (A + k_{N_2} N_{N_2} + k_{O_2} N_{O_2} + k_{3-B} N_{O_2} N_T)$$

At 580 torr, the predicted value is $\eta_F = 7.2 \times 10^{-6}$, which is in excellent agreement with the measurements of Davidson and O'Neil [DO64] and Mitchell [Mi70]. At 760 torr, the predicted value is $\eta_F = 5.2 \times 10^{-6}$. The fluorescence efficiency decreases slightly more rapidly than p^{-1} between 580 and 760 torr because of the three-body quenching term.

A similar prediction of the fluorescence efficiency for the second positive emission bands can be made, starting with the $v'=0 \rightarrow v''=0$ transition at 337.1 nm. The low pressure fluorescence efficiency in air is $\eta_{F_0} = (1.5 \pm 0.2) \times 10^{-3}$ [Ha68, OD69, Mi70, KK73, KK79]. The radiative decay rate is 2.55×10^7 [DR82], and quenching rates for $N_2(C, v=0)$ are $(1.2 \pm 0.15) \times 10^{-11} \text{ cm}^3/\text{s}$ by N_2 and $3.0 \times 10^{-10} \text{ cm}^3/\text{s}$ by O_2 [BD67, OD69, Mi70, CA71, MSB73, ABB74]. These parameters lead to values of $\eta_F = (2.2 \pm 0.3) \times 10^{-5}$ at 760 torr and $(3.1 \pm 0.4) \times 10^{-5}$ at 580 torr.

The second positive $v'=0 \rightarrow v''=3$ transition at 406.0 nm that we monitor has the same upper state as the 337.1-nm transition, and so its fluorescence efficiency is related to the values above by the relative radiative transition rate of 0.109. This gives $\eta_F = 2.4 \times 10^{-6}$ at 760 torr and $\eta_F = 3.4 \times 10^{-6}$ at 580 torr.

The combination of the above parameters leads to prediction of the signal levels at 580 torr of 2.2 mV/A at 391.4 nm and 0.38 mV/A at 406.0 nm, applicable when the PMT's are operated at a gain of 1×10^6 . The predicted values will vary with pressure; this variation is shown graphically in comparisons with the experimental results in the next section.

III RESULTS

Absolute 391.4-nm Emission

All our measurements of 391.4-nm emission have been normalized to a PMT gain of 1×10^6 , and each signal has been divided by the current on a micropulse-by-micropulse basis using the beam current data provided in Table III of [BMP83]. This gives normalized signals in mV/A for direct comparison with the predictions of Section II. The results are presented two ways. Figures 6 through 12 present signals versus micropulse number for each pressure (5, 10, 30, 50, 100, 300, and 580 torr). These plots allow easy examination of the variation of fluorescence efficiency with pulse number (or current) at each pressure. The predicted signal level is also indicated on each plot.

In the majority of cases, the measurements are in good agreement with the predictions, typically within $\pm 50\%$. There are two exceptions: (1) the measured signals for the first two micropulses are generally higher than expected, and (2) the signals for the late micropulses at low pressures tend to drop below the predicted values. We believe that the first discrepancy is simply a signal-to-noise problem because we are dividing a small intensity signal by a small current, which can give large scatter. Also, any x-ray-induced signals will cause a larger perturbation toward larger signals during the first few micropulses where the channel emission signals are smaller. Note that there is no evidence for an enhancement in signal with increasing pulse number for pulses 1 through 3 as reported by Karl and Buchwald [KB84]. On the contrary, our data show decreasing normalized signals over the same pulse intervals.

The second discrepancy is more puzzling. One possible but unlikely explanation is that the reduced emission is caused by a reduction in channel density due to hole boring by the earlier micropulses. A second possibility is that the beam does not propagate well at the lower pressures so that some current is "scraped off" on the collimator located at the beam exit (Figure 3).

The second way to present the data is signal versus pressure for each micropulse, as in Figures 13 through 21. Again, the predicted signals are shown on each graph. The data for micropulses 1 and 2 again show the large scatter and the larger values than predicted that were noted above. The measured values for micropulses 3 through 6 are in good agreement with the predicted values, with no significant evidence of enhancements. Micropulses 7 through 9 show the progressively greater decrease of intensities at the lowest pressure. Figure 22 presents a superposition of the data for all the micropulses as a function of pressure together with the mean and standard deviation at each pressure. The mean values are in excellent agreement with predictions. The deviations are not completely random scatter: the high values are mostly from micropulses 1 and 2, whereas the low values at low pressures are from micropulses 7 - 9.

Absolute 406.0-nm Emission

Figures 23 through 29 present intensity signals versus micropulse number at each of the pressures studied. Each signal is divided by the current for that micropulse and is normalized to a PMT gain of 1×10^6 . Again, the predicted value is shown on each plot. For pressures above 50 torr, the measurements are clustered around the predictions for all micropulses (although the scatter is greater for the early and late micropulses because these signals are intrinsically smaller), indicating that there is again no enhancement by self-induced-field plasma excitation. However, at lower pressures, that is no longer true. Enhancements of as much as a factor of 4 occur; the enhancements are largest for pulses 3 and 4, which typically have the highest currents.

The same data are presented as normalized signal versus pressure for each micropulse in Figures 30 through 38, together with the predicted values. This presentation clearly shows the agreement between experiments and predictions for $p > 50$ torr and the enhancements at lower pressures. Figure 39 combines the data for all micropulses together with mean and standard deviations and shows the consistency of the observed effect.

Vibrational Temperatures

As described in Section II, simultaneous measurements of the 391.4- and 423.6-nm emissions were taken. These signals were normalized to PMT gains of 1×10^6 , and the ratios of signals were then calculated on a micropulse-by-micropulse basis. The results are presented in Figures 40 through 46. On the right-hand side of each plot is a T_V scale that corresponds to the signal ratio as determined from the shock tube tests. A great deal of scatter occurs in the data, largely due to forming the ratio by dividing by small 423.6-nm signals that have significant scatter. For the more numerous 580-torr data, we present the mean and standard deviation for each micropulse.

There is an inconsistency between the largest ratios measured in these tests (~ 7) and the largest ratio determined in our Febetron calibration experiments (~ 5). We have also measured the larger ratios in experiments at the ETA facility at LLNL, which suggests that the Febetron calibration experiments are subject to some systematic error (see the discussion on this point in Section II). Therefore, we must settle for qualitative results at this point.

The trend of the data is that the signal ratio decreases systematically with each micropulse and that the decrease is somewhat more pronounced at lower pressures. For example, the decrease is about 40% at 580 torr and about 60% at 5 torr (the scatter is really too great to extract too much detail from these results). Similar decreases in the temperature calibration curve correspond to vibrational temperatures of ~ 750 K at the higher pressure and ~ 1400 K at the lower pressure. Recall that the calculated maximum vibrational temperature if all the beam-deposited energy went into vibration is about 1900 K.

If the T_V increase is in fact greater at low pressure than at high, it could easily be due to additional electronic and/or vibrational excitation by the self-induced-field plasma current. We have already seen that this enhances the second positive emission (406.0 nm) at low pressures, and vibrational excitation occurs at even lower plasma electron energies.

Rotational Temperatures

Rotational temperatures are determined from the ratios of 406.0/403.0-nm signals. In all the tests, the 403.0-nm signals were very small, typically corresponding to 1 or 2 photoelectrons per micropulse. X-ray-induced background signals are frequently equal to or larger than the light signals. We therefore feel that it is meaningful to report results only for conditions where we have several shots that allow data averaging, and this was only the case at 580 torr. The mean and standard deviations of the 406.0/403.0 ratios for each micropulse at that pressure are presented in Figure 47; again, we have put a rotational temperature scale on the right-hand side of the graph that is based on the shock-tube calibrations. Although the standard deviations are large, the mean values for micropulses 2 through 9 are in good agreement with the expected ratio for $T_R = 300$ K.

We estimated in Section I that the maximum temperature rise due to direct beam energy deposition was ~ 130 K, but also pointed out that most of this energy produces ionization and electronic excitation. The energy cascade to the vibrational degrees of freedom is fast enough to occur during the pulse train, but the subsequent vibrational relaxation should require 0.1 to 100 ms (see Section I). Thus, we do not expect to measure a significant rotational temperature rise during the pulse train. The results of Figure 47 are consistent with this expectation, although it is not appropriate to draw an unequivocal conclusion in view of the scatter in the data.

Far-Field Emission Measurements

In the far-field emission measurements we used a single PMT viewing the open-air beam path over the first 6-7 m of propagation distance. A filter placed in front of the PMT selected measurement of either the 391.4-nm or the 337.1-nm transition. Typical intensity histories at each wavelength are presented in Figure 48. The results at both wavelengths are very similar. They show the appearance of each micropulse, integrating the total induced fluorescence as the beam emerges into air. The total light from each micropulse partially decays as the beam propagates across the field of view and is extinguished as the beam disappears behind the bunker that limits the

downstream field of view. Each micropulse is just disappearing as the next micropulse appears.

The decay of intensity from each micropulse, even in the first 6 m of propagation, is surprising because the stopping distance for 25-MeV electrons in 580 torr air should be greater than 100 m (measurements by Chu [Ch84] apparently are consistent with the longer propagation). As we pointed out in Section II, we were not able to experimentally verify that the response of our detection system was uniform over the entire 6-m path, but we have no reason to suspect that it was not.

The decay of intensity during the 6-m propagation distance increases with increasing micropulse number, being about 30% for the first micropulse and about 50% for the later micropulses. This suggests that the later micropulses did not propagate as well as the earlier ones, perhaps due to residual conductivity effects in the air channel. If we assume the decays are exponential, then the light signals would decay to 5% of their peak values in approximately 60 m for the initial pulses and approximately 30 m for the later ones.

The peak signals for the strongest micropulses are typically 650 mV for 391.4 nm and 400 mV for 337.1 nm. We can calculate the expected values based on the energy deposition, fluorescence efficiency, and photomultiplier response parameters quoted above, together with the appropriate geometric factors for this setup. This results in predicted signals of 570 mV at 391.4 nm and 310 mV at 337.1 nm. Thus, the measurements and predictions agree to within 15% at 391.4 nm and to within 30% at 337.1 nm. Furthermore, the ratio of 391.4/337.1-nm signals was measured to be 1.63 and is predicted to be 1.84, so again the agreement is to within 13%. (Note that the actual intensity at 337.1 nm is about 4 times the intensity at 391.4 nm; the signal ratio was reversed because the PMT was operated at much lower gain for the 337.1-nm measurements.)

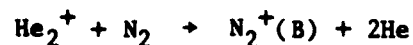
Search for Superradiant Emission

There is considerable speculation whether atmospheric-pressure air pumped by an intense relativistic electron beam will achieve population inversions on either the N_2^+ first negative or the N_2 second positive bands, both of which undergo lasing under other pumping conditions. If inversions did occur, one might expect superradiant emission to build up in the direction of beam

motion, with a resulting intense, collimated light propagating along the beam path. To check this possibility in a very qualitative way, we mounted a fluorescent screen (a white bedsheet coated with spray starch) in the beam path about 15 m downstream from the exit foil. Several observers watched this screen during a number of night-time tests. We assumed that a localized, circular, bright fluorescent spot would indicate superradiant emission, but saw no evidence of such a spot. Rather, the entire screen fluoresced nearly uniformly; this could result either from diffuse electrons hitting the screen (the calculated Bennett radius at 15 m is ~ 1 m [BMP83]) or from isotropic uv radiation hitting the screen and inducing secondary fluorescence.

An absence of superradiance is not surprising. Although 337.1-nm laser action has been produced by pumping N_2 with intense electron beams [DH72, PGJ72, Pa73], lasing action in each case was confined to gas pressures below 50 torr. McArthur and Poukey have attributed the pumping to excitation by plasma electrons drifting in the self-induced electric field produced by the beam [Pa73, MP74, MP75]. Achievement of E/p values high enough to produce the excitation requires either low p (as in the referenced experiments) or very high induced fields. Although our measurements of the second-positive emission (406.0 nm) indicate plasma excitation at pressures below 50 torr, there is no evidence of such excitation at local atmospheric pressure where the superradiance experiment took place. In contrast to pumping by electron beams, lasing at 337.1 nm in atmospheric pressure air has been observed using spark discharge excitation [SHN68].

Lasing or superradiant emission on the first negative bands at 391.4 or 427.8 nm has apparently never been observed in pure N_2 (or air) although it occurs quite readily in very dilute mixtures of N_2 in helium [CCC74]. In the latter case, the excitation is due to the efficient resonant charge transfer



IV CONCLUSIONS

On the basis of experiments described in this report, we draw the following conclusions:

First Negative Emission (391.4 nm)

The 391.4-nm emission was approximately linear with beam current for all micropulses at all pressures. The fluorescence efficiencies agreed with previously measured values to within experimental accuracy in all cases.

The only minor exception was an observed decrease of signal levels for later micropulses in each pulse train at pressures of 30 torr and below.

Second Positive Emission (406.0 nm, 337.1 nm)

The 406.0-nm emission was linear with beam current and had the expected fluorescence efficiency for all micropulses and at all pressures above 50 torr. At 50 torr and lower pressures, the intensity was enhanced (by as much as a factor of 4), with the enhancement increasing at lower pressures. The enhancement was proportional to beam current, reaching a maximum on micropulses 3-4.

The enhancement was completely consistent with previous observations of excitation by plasma electrons accelerated in the self-induced electric field produced by the beam. If the enhancement can be quantified, it offers a means of measuring the induced electric field by simple, nonintrusive, remote optical techniques.

Vibrational Temperatures

The scatter in these data is rather large, but there is a consistent trend indicating an increase of T_v throughout each pulse train. The temperature rises to about 750 K at higher pressures and to about 1400 K at lower pressures. The higher figure corresponds approximately to 70% relaxation into vibration of all energy directly deposited by the electron beam.

Rotational Temperatures

Because our 403.0-nm signals were so small in these experiments, we are able to report results only at 580 torr, where we have enough shots for data averaging. In that case, it appears that the rotational temperature stays approximately at $T_R = 300$ K.

Far-Field Propagation Measurements

The maximum signals observed at 391.4 and 337.1 nm were in excellent agreement with predicted values. The signals decayed by 30% to 50% as the micropulses propagated within the field of view, which was limited to ~ 7 m. This unexpected result suggests that the beam propagates only about 60 m before the light intensity decreases to 5% of peak values. These results are in disagreement with measurements by Chu [Ch84].

Superradiant Emission

We observed no evidence for superradiant emission in our observations, which were confined to local atmospheric pressure of 580 torr.

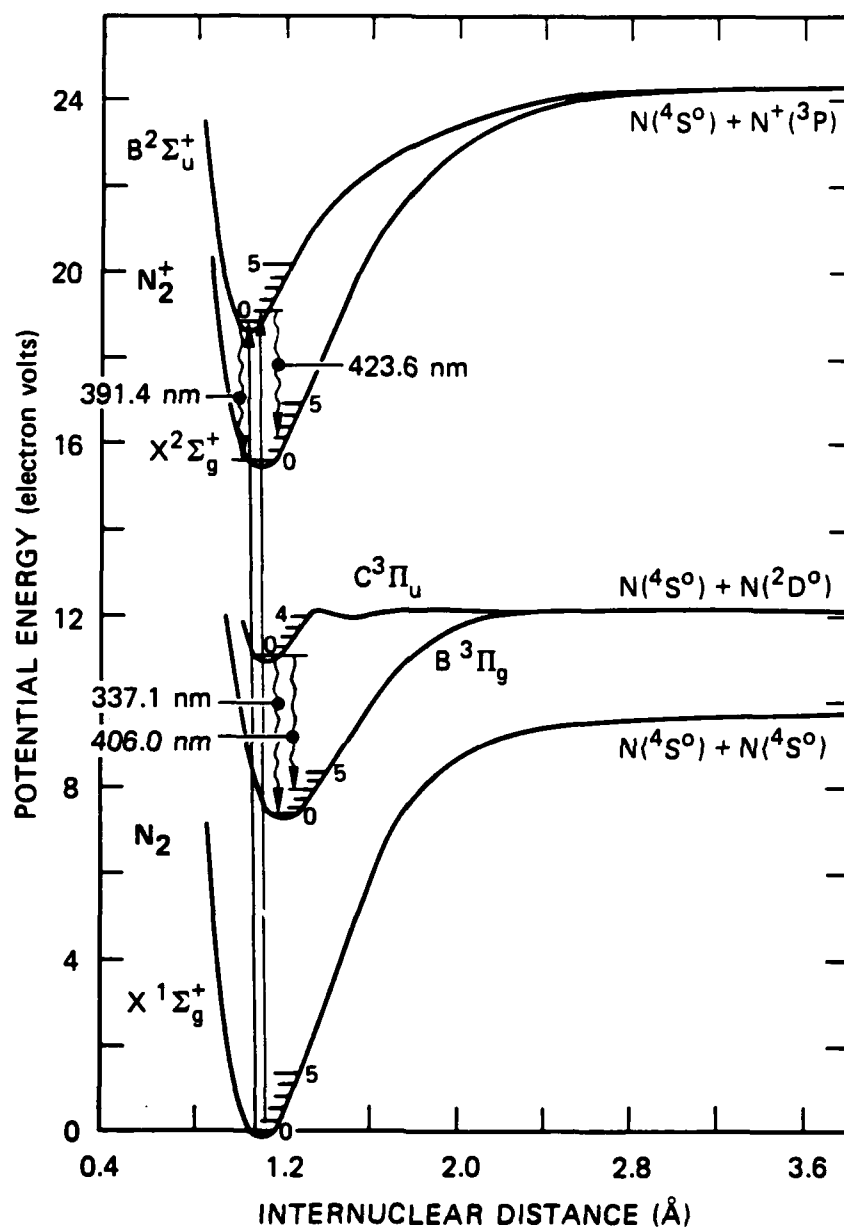
Summary

Because the beam current in these tests was only about 40% of the expected value and because the x-ray-induced signals were somewhat more severe than previously experienced, our signal-to-noise ratios were not as good as desired. However, we accomplished most of our measurement objectives. In general, the optical emissions behaved very much as expected, and there were few surprises. Optical studies continue to be a valuable means of beam and air channel diagnostics, and additional information can be gained as we continue to quantify the emissions.

REFERENCES

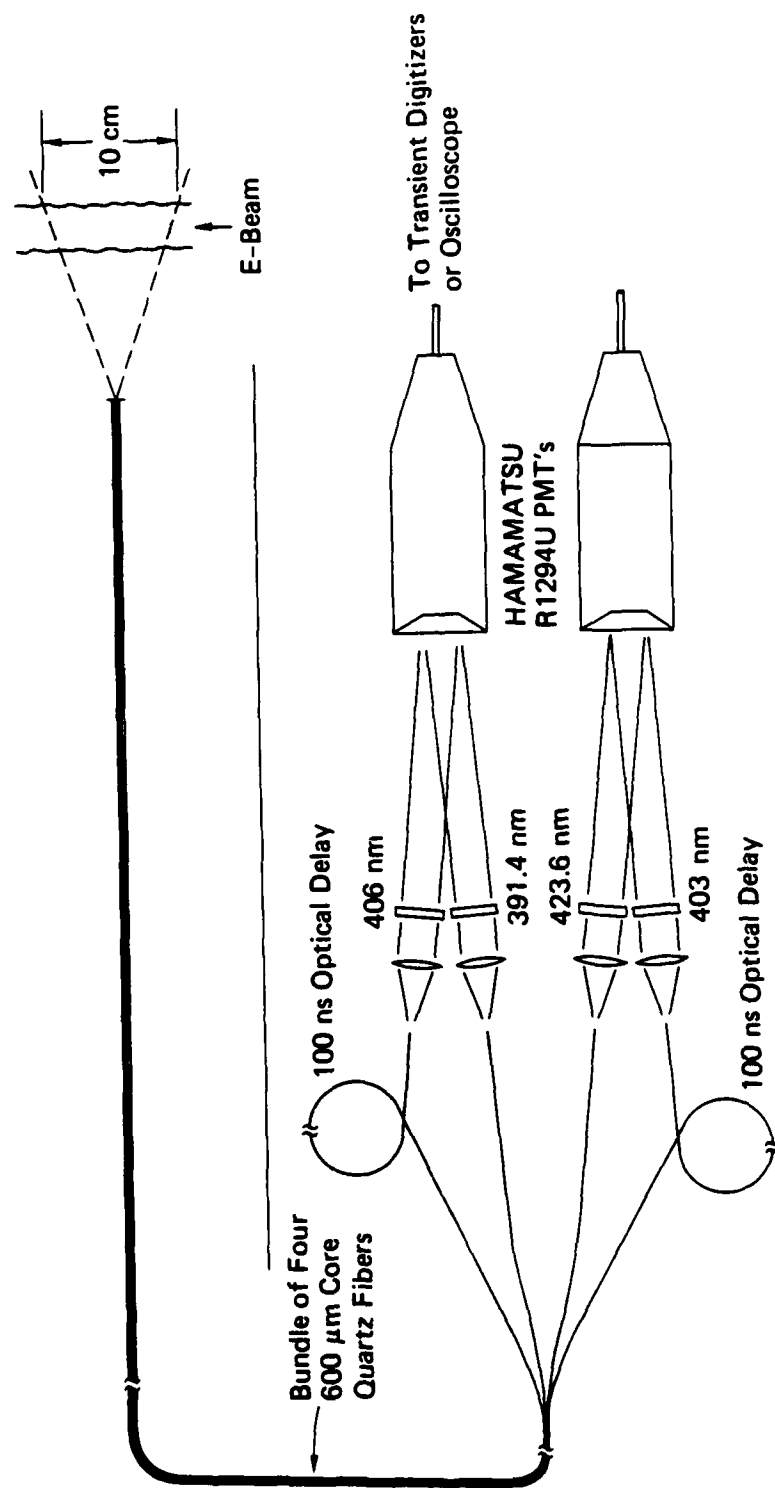
- ABB74 F. Albugues et al., J. Chem. Phys. 61, 2695 (1974).
- BD67 B. Brocklehurst and F. A. Downing, J. Chem. Phys. 46, 2976 (1967).
- BMP83 L. A. Buita, D. C. Moir, E. W. Pogue, and T. P. Starke, "Los Alamos PHERMEX Banda Final Report," Los Alamos National Laboratory Report No. M-4:GR-83-10 (October 26, 1983). SECRET.
- CA71 J. M. Calo and R. C. Axtmann, J. Chem. Phys. 54, 1332 (1971).
- CCC74 C. B. Collins et al., Appl. Phys. Lett. 24, 477 (1974).
- Ch84 K. Chu (Sandia National Laboratory), presented at the Particle Beam Panel Meeting, Los Alamos National Laboratory, February 29, 1984.
- CS71 F. J. Comes and F. Speier, Chem. Phys. Lett. 4, 13 (1969); Zeitsch. Naturforschung 26a, 1998 (1971).
- DH72 R. W. Dreyfus and R. T. Hodgson, Appl. Phys. Lett. 20, 195 (1972).
- DO64 G. Davidson and R. O'Neil, J. Chem. Phys. 41, 3946 (1964).
- DR82 M. N. Dumont and F. Remy, J. Chem. Phys. 76, 1175 (1982).
- Ha68 P. L. Hartman, Planet. Space Sci. 16 1315 (1968).
- HB56 G. J. Hine and G. L. Brownell, Radiation Dosimetry (Academic Press, New York, 1956).
- H180 R. M. Hill, "Optical Emissions from Shock-Heated Air Excited by Relativistic Electrons (U)," Final Report, Task 3.7, Contract F08606-78-C-0032 (April 1980), SRI O-4229. SECRET.
- HPE70 M. N. Hirsh, E. Poss, and P. N. Eisner, Phys. Rev. A 1, 1615 (1970).
- KB84 R. R. Karl and M. I. Buchwald (Los Alamos National Laboratory), presented at the Particle Beam Panel Meeting, Los Alamos National Laboratory, February 29, 1984.
- KH74 A. E. Kassem and R. S. Hickman, Phys. Fluids 14, 2543 (1971).
- KK73 S. P. Khare and A. Kumar, Planet. Space Sci. 21, 1381 (1973).
- KK79 S. P. Khare and A. Kumar, Indian J. Radio Space Phys. 8, 122, (1979).
- La73 R. A. Langley, J. Chem. Phys. 58, 3675 (1973).
- LW69 J.W.L. Lewis and W. D. Williams, AIAA J. 7, 1202 (1969).
- M170 K. B. Mitchell, J. Chem. Phys. 53, 1795 (1970).
- MM71 G. I. Mackay and R. E. March, Can. J. Chem. 49, 1268 (1971).

- MP74 D. A. McArthur and J. W. Poukey, Phys. Rev. Lett. 32, 89 (1974).
- MP75 D. A. McArthur and J. W. Poukey, IEEE J. Quant. Elect. QE-11, 892 (1975).
- MSB73 P. Millet et al., J. Chem. Phys. 58, 5839 (1973).
- OD69 R. O'Neil and G. Davidson, in Atmospheric Emissions, ed. by B. M. McCormac and A. Omholt (Van Nostrand Reinhold Co., New York, 1969).
- OPH74 R. R. O'Neil et al., J. Geophys. Res. 79, 1942 (1974).
- Pa73 E. L. Patterson, J. Appl. Phys. 44, 3193 (1973).
- PGJ72 E. L. Patterson, J. B. Gerardo, and A. W. Johnson, Appl. Phys. Lett. 21, 293 (1972).
- RD78 F. Remy and M. N. Dumont, J. Quant. Spectrosc. Radiat. Transfer 20, 217 (1978).
- SD83 T. P. Starke and K. A. Dreyer, "Project Banda Preliminary Report (U)", Los Alamos National Laboratory Report No. M-4:GR-83-9 (Sept. 30, 1983). SECRET.
- SHN68 A. Svedberg, L. Hogberg, and R. Nilsson, Appl. Phys. Lett. 12, 102 (1968).
- SHS70 A. T. Stair, Jr. et al., in The Radiating Atmosphere, ed. by B. M. McCormac (D. Reidel Pub. Co., 1970).
- SH71 F. Shelby and R. A. Hill, Phys. Fluids 14, 2543 (1971).
- St83 T. P. Starke, IEEE Trans. Nucl. Sci. NS-30, 1402 (1983).
- TWF72 J. B. Tellinghuisen et al., J. Chem. Soc. Faraday Trans. II 68, 833 (1972).



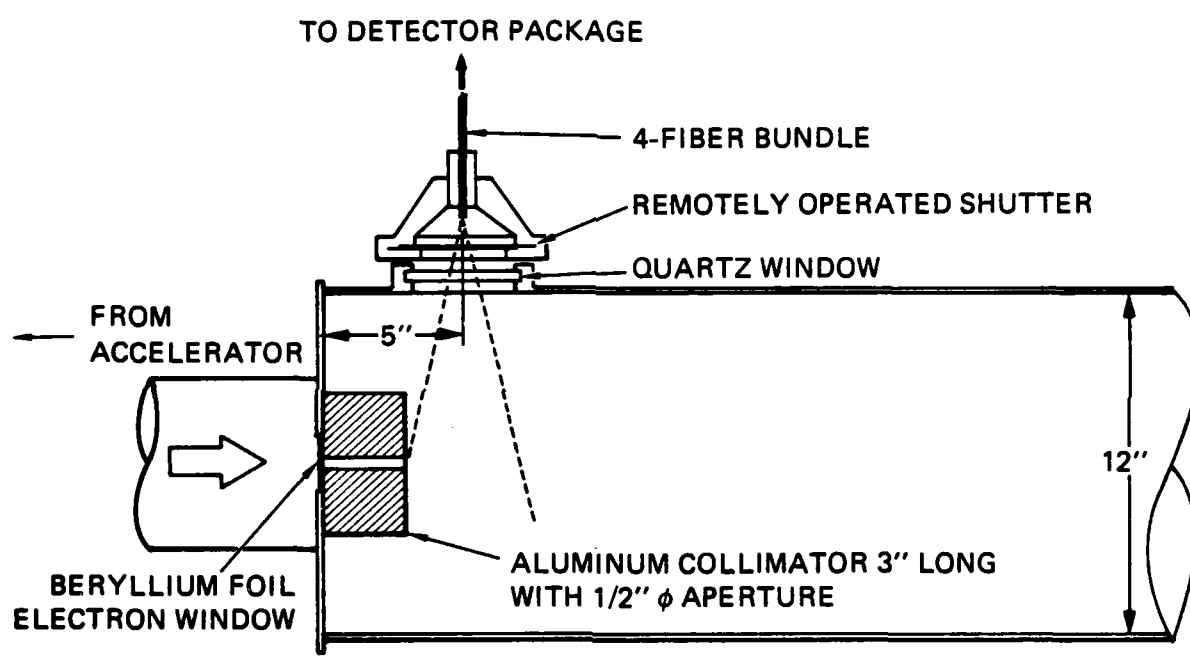
JA-2690-103

FIGURE 1 ELECTRONIC STATES OF N_2 AND N_2^+ RELEVANT TO OPTICAL BEAM DIAGNOSTICS



JA-2690-44A

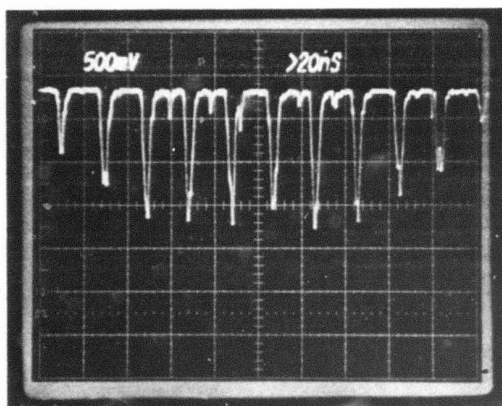
FIGURE 2 OPTICAL LAYOUT FOR TEMPERATURE MEASUREMENTS (MOD 2)



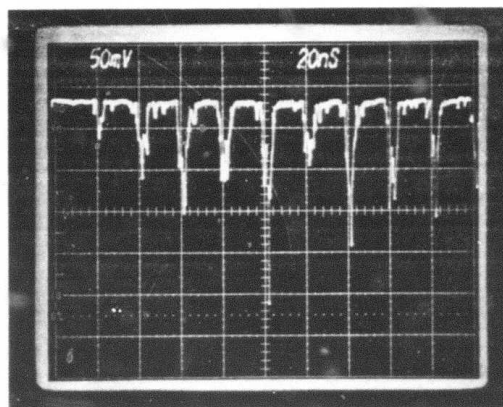
JA-2690-83

FIGURE 3 SETUP FOR OPTICAL MEASUREMENTS AT PHERMEX

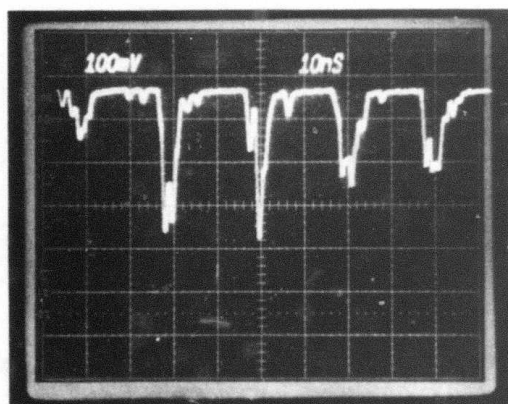
391.4 nm



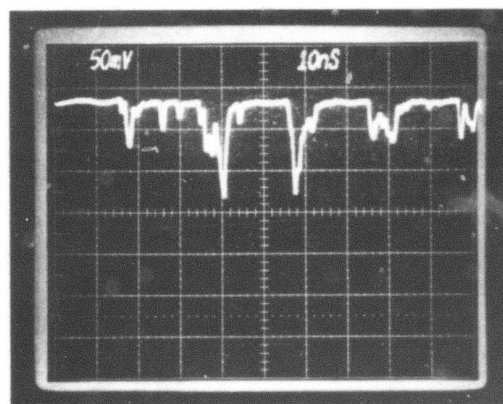
423.8 nm



406.0 nm

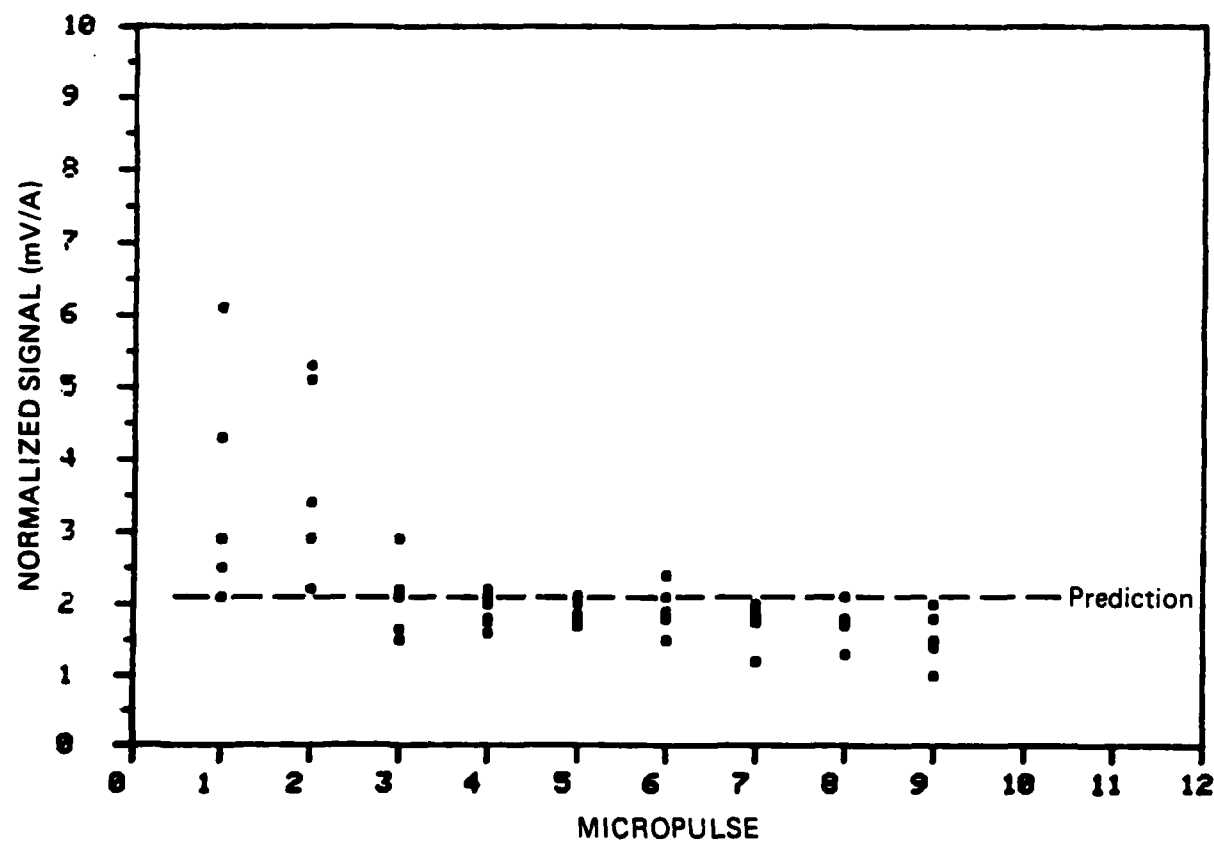


403.0 nm



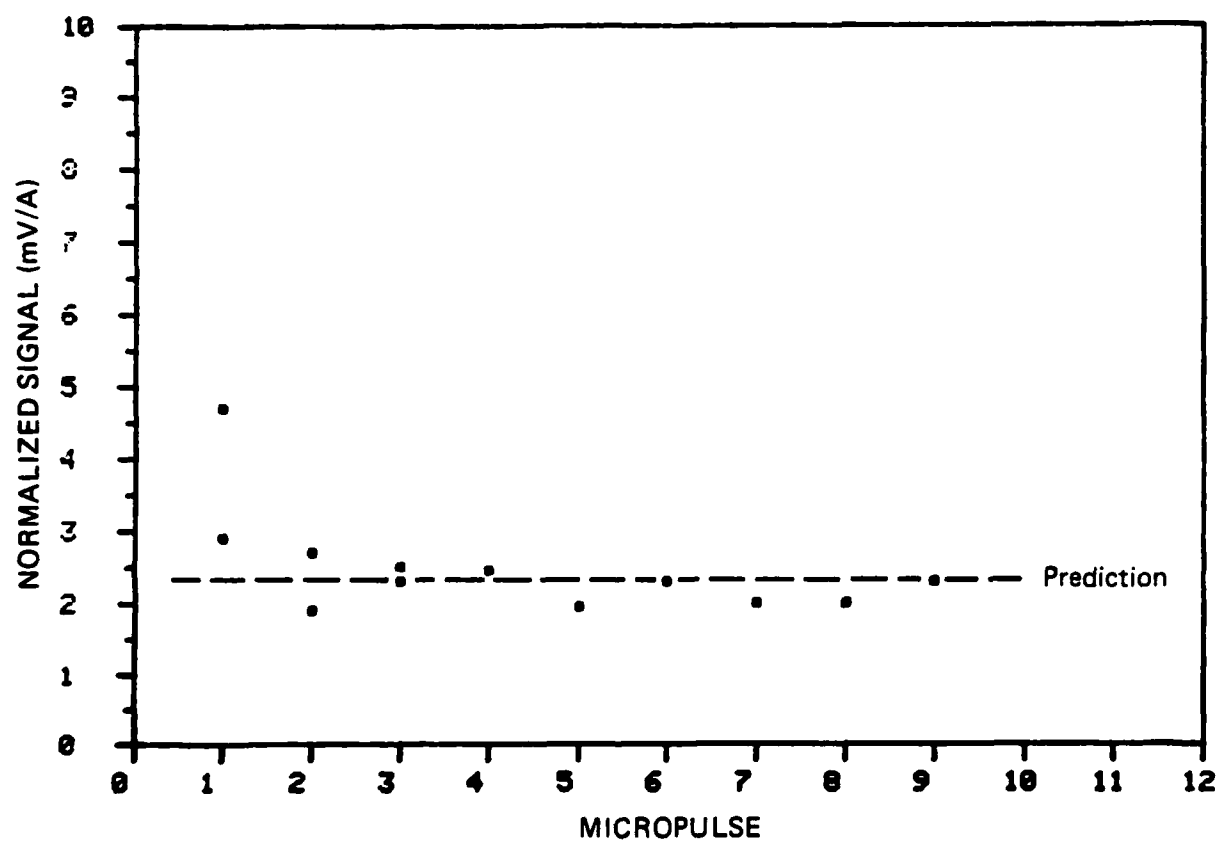
JP-2690-87A

FIGURE 4 TYPICAL INTENSITY HISTORIES FOR PHERMEX EXCITING
AIR AT 580 torr



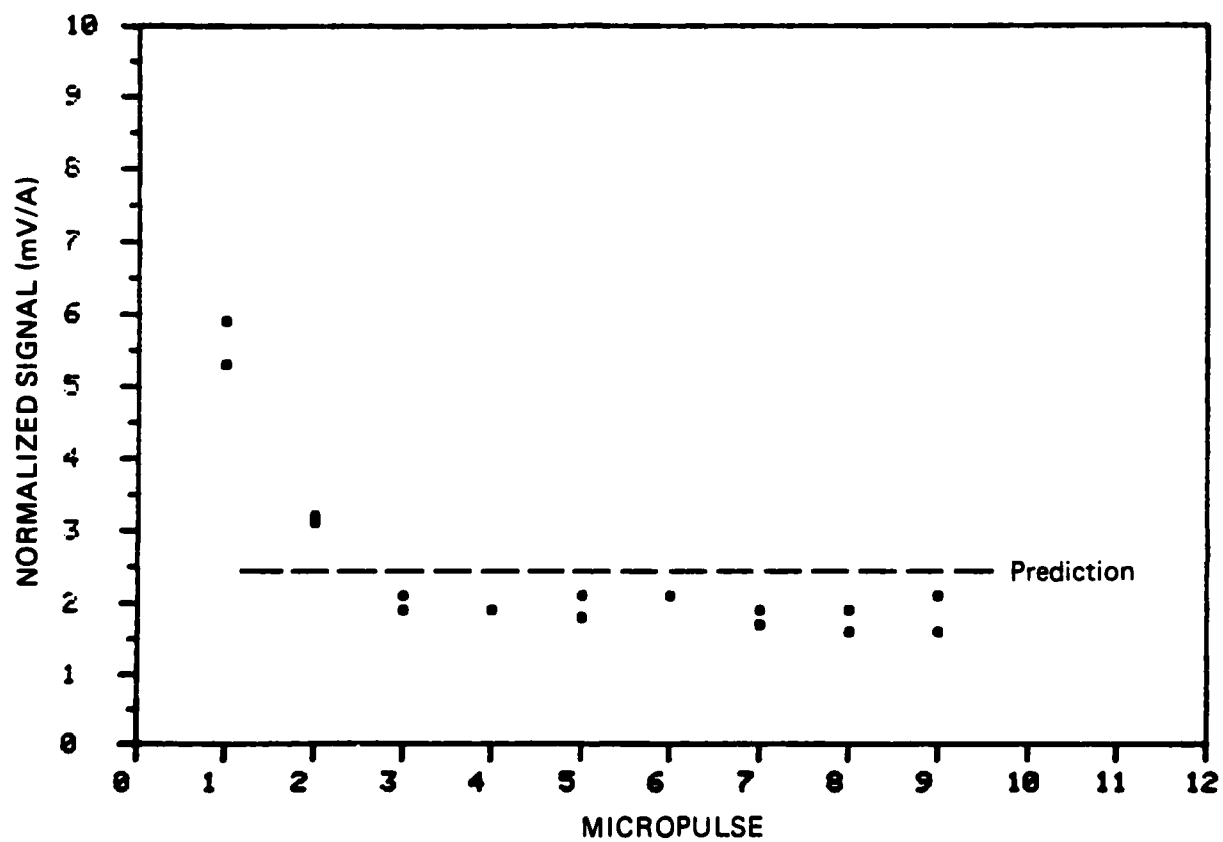
JA-2690-105

FIGURE 6 NORMALIZED 391.4-nm SIGNALS VERSUS MICROPULSE AT 580 torr



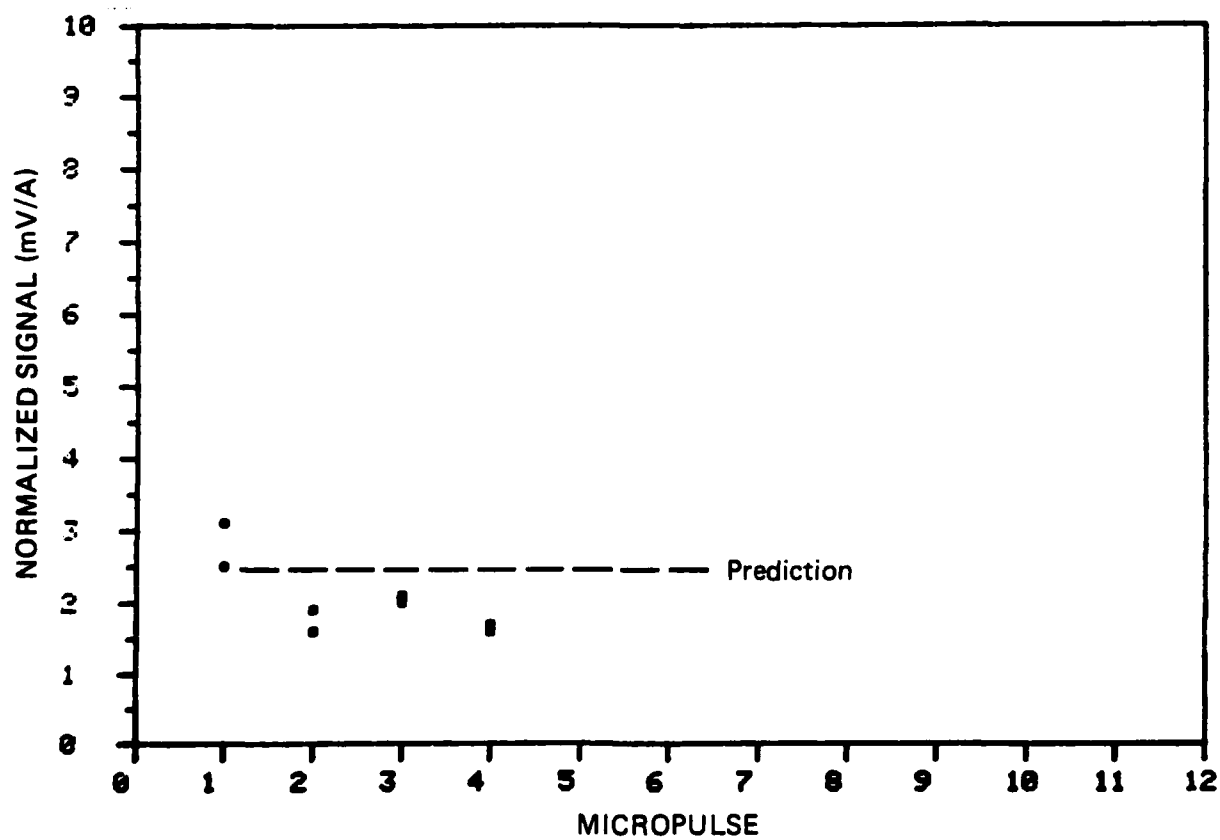
JA-2690-106

FIGURE 7 NORMALIZED 391.4-nm SIGNALS VERSUS MICROPULSE AT
300 torr



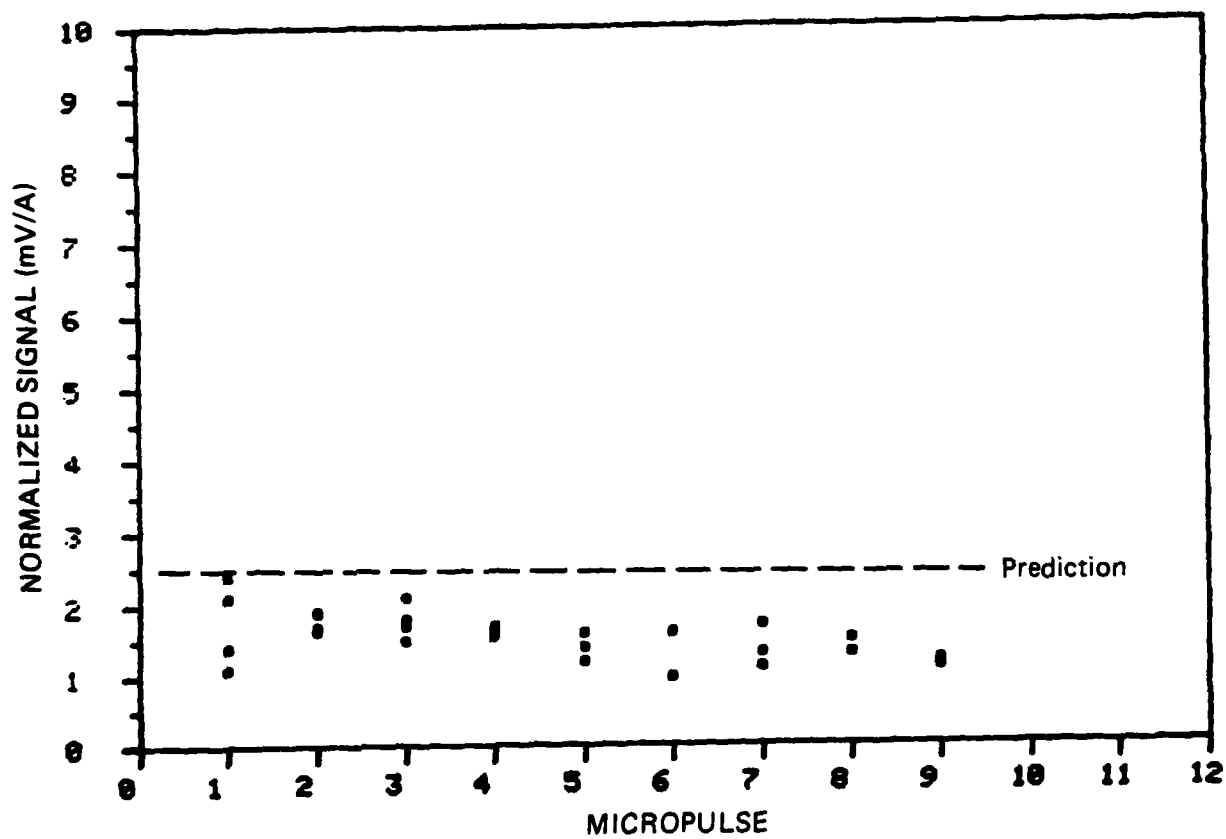
JA-2690-107

FIGURE 8 NORMALIZED 391.4-nm SIGNALS VERSUS MICROPULSE AT 100 torr



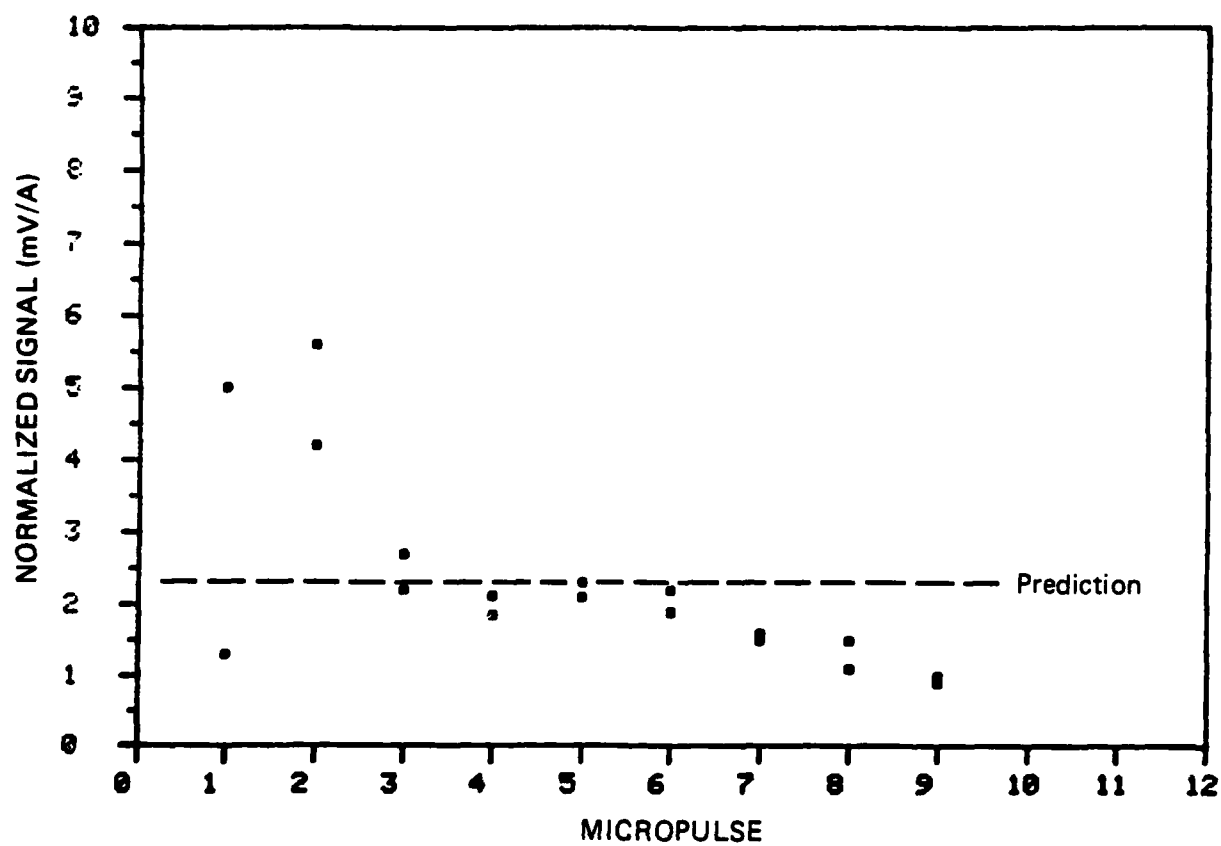
JA-2690-108

FIGURE 9 NORMALIZED 391.4-nm SIGNALS VERSUS MICROPULSE AT
50 torr



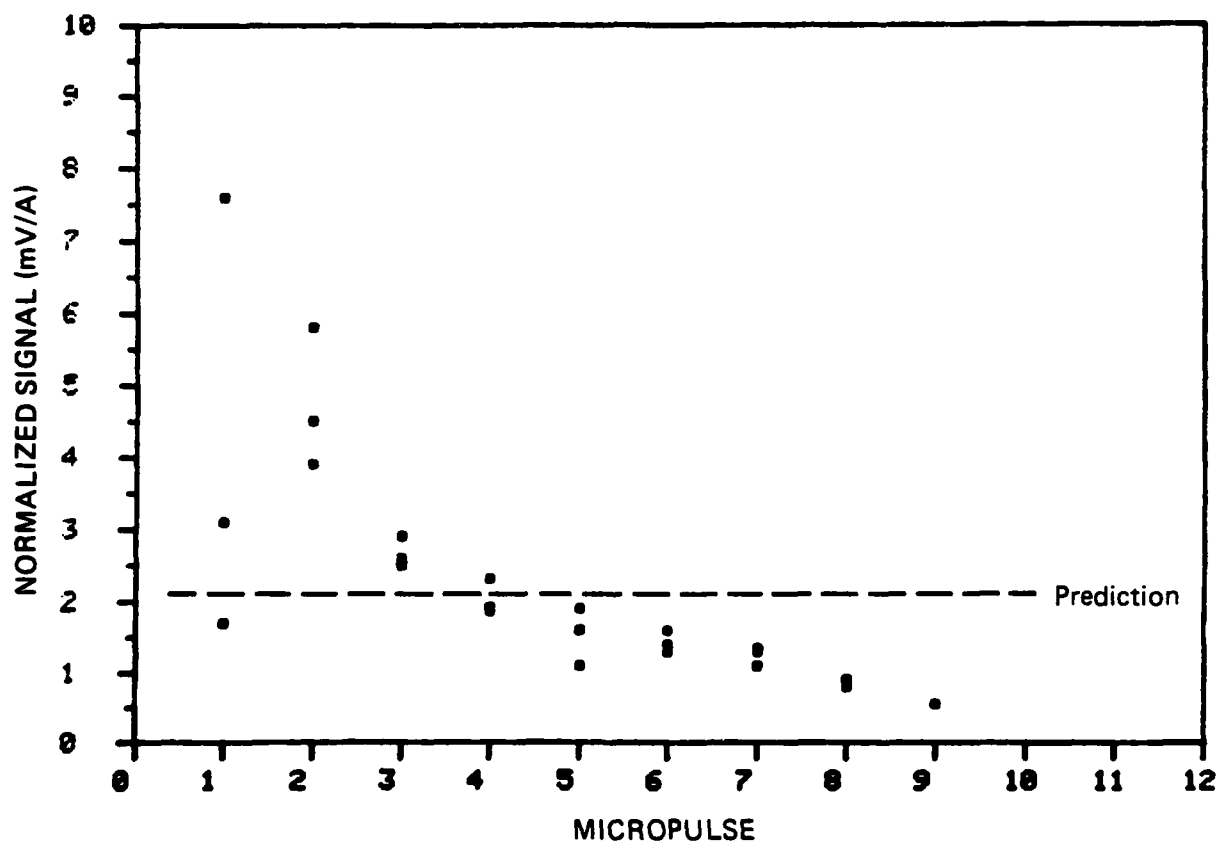
JA-2690-109

FIGURE 10 NORMALIZED 391.4-nm SIGNALS VERSUS MICROPULSE AT
30 torr



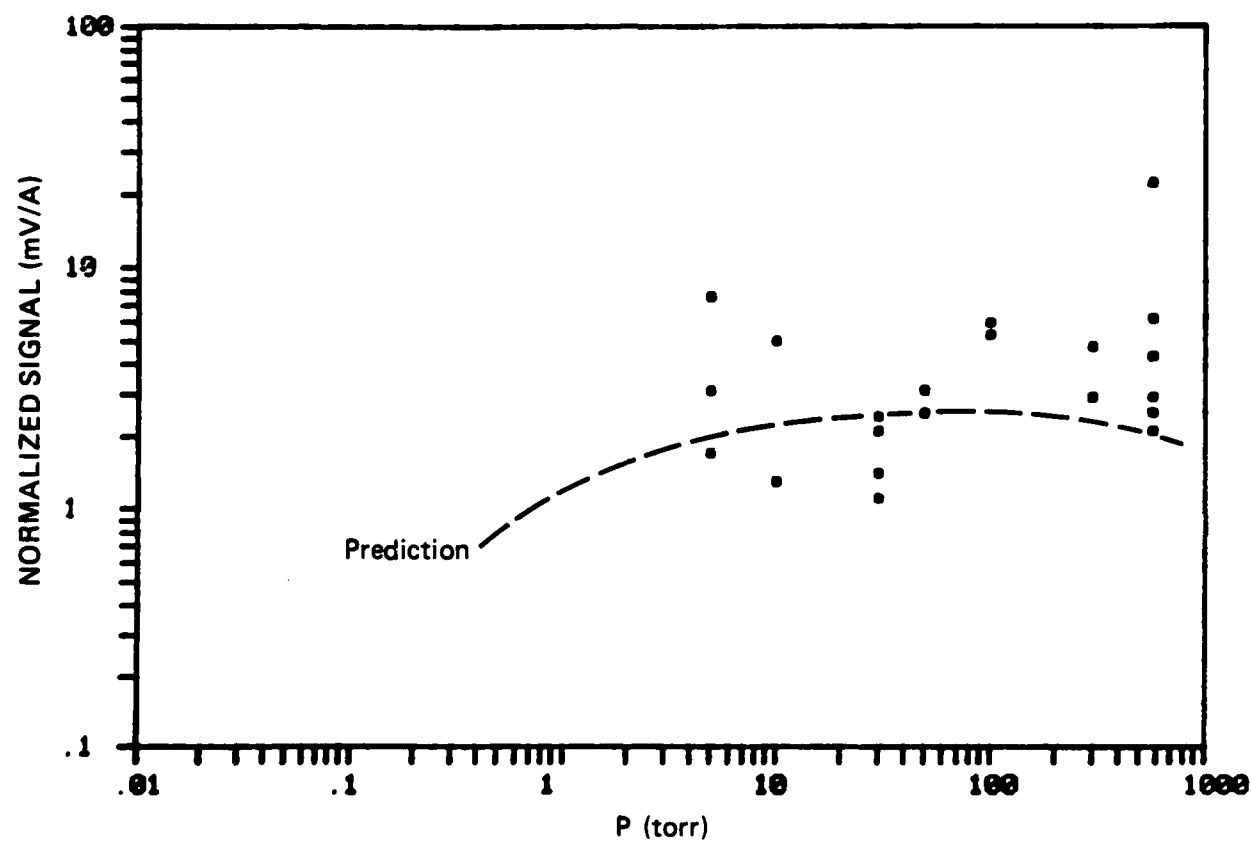
JA-2690-110

FIGURE 11 NORMALIZED 391.4-nm SIGNALS VERSUS MICROPULSE AT 10 torr



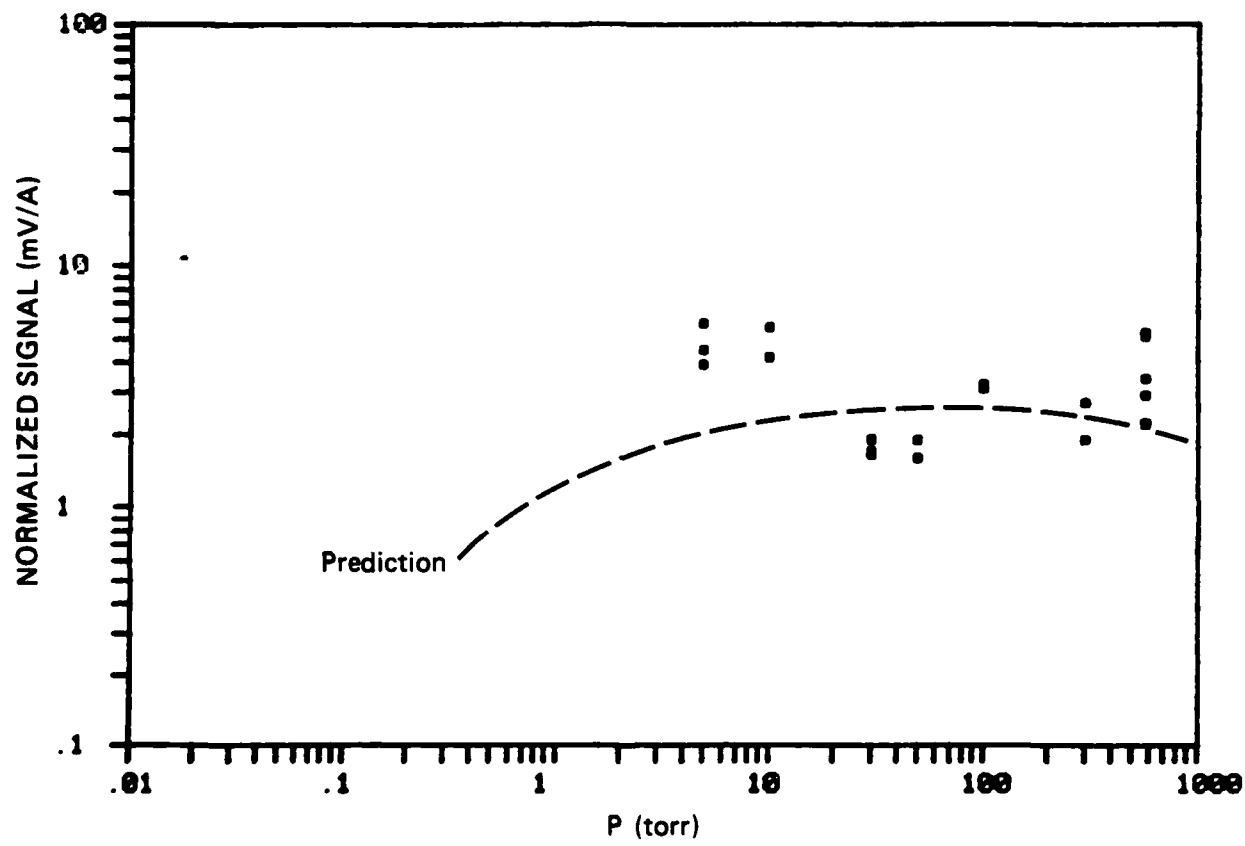
JA-2690-111

FIGURE 12 NORMALIZED 391.4-nm SIGNALS VERSUS MICROPULSE AT 5 torr



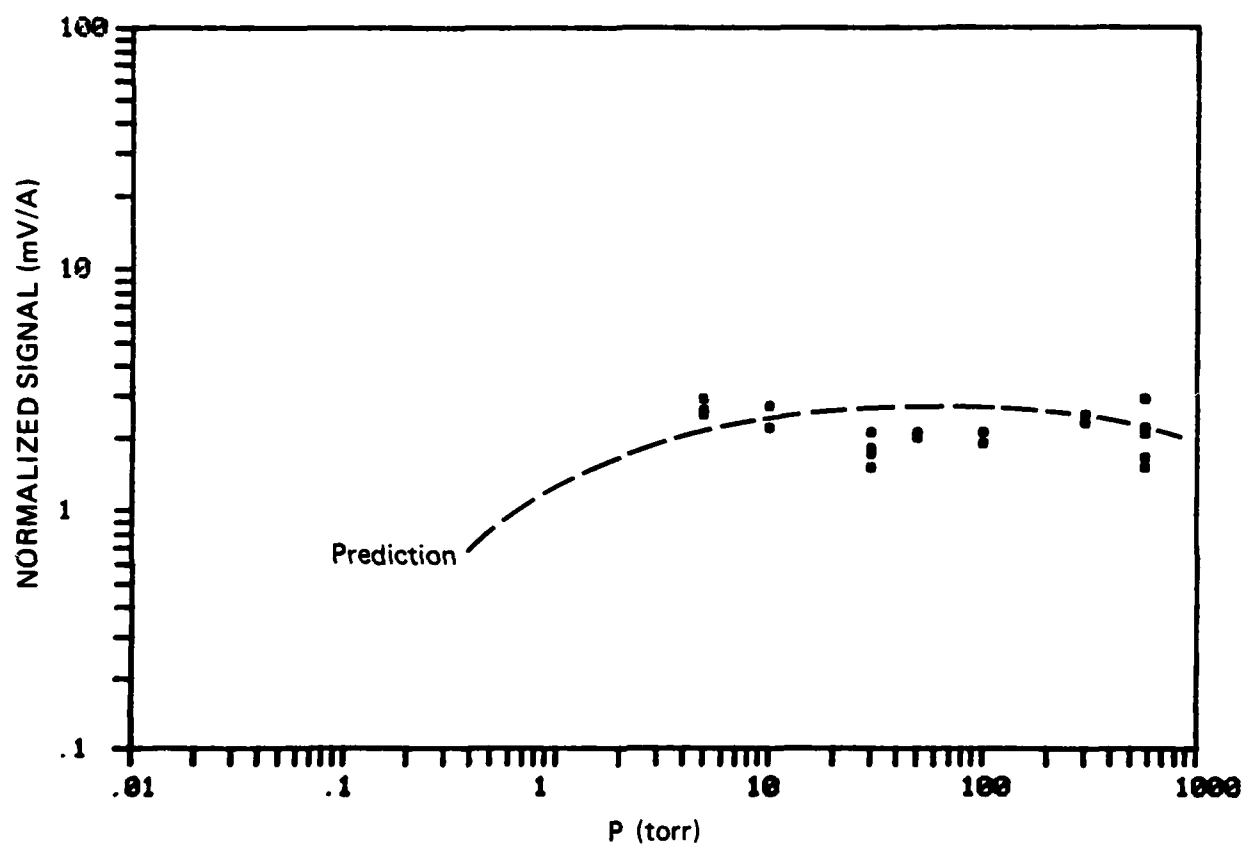
JA-2690-112

FIGURE 13 NORMALIZED 391.4-nm SIGNALS VERSUS PRESSURE
FOR MICROPULSE No. 1



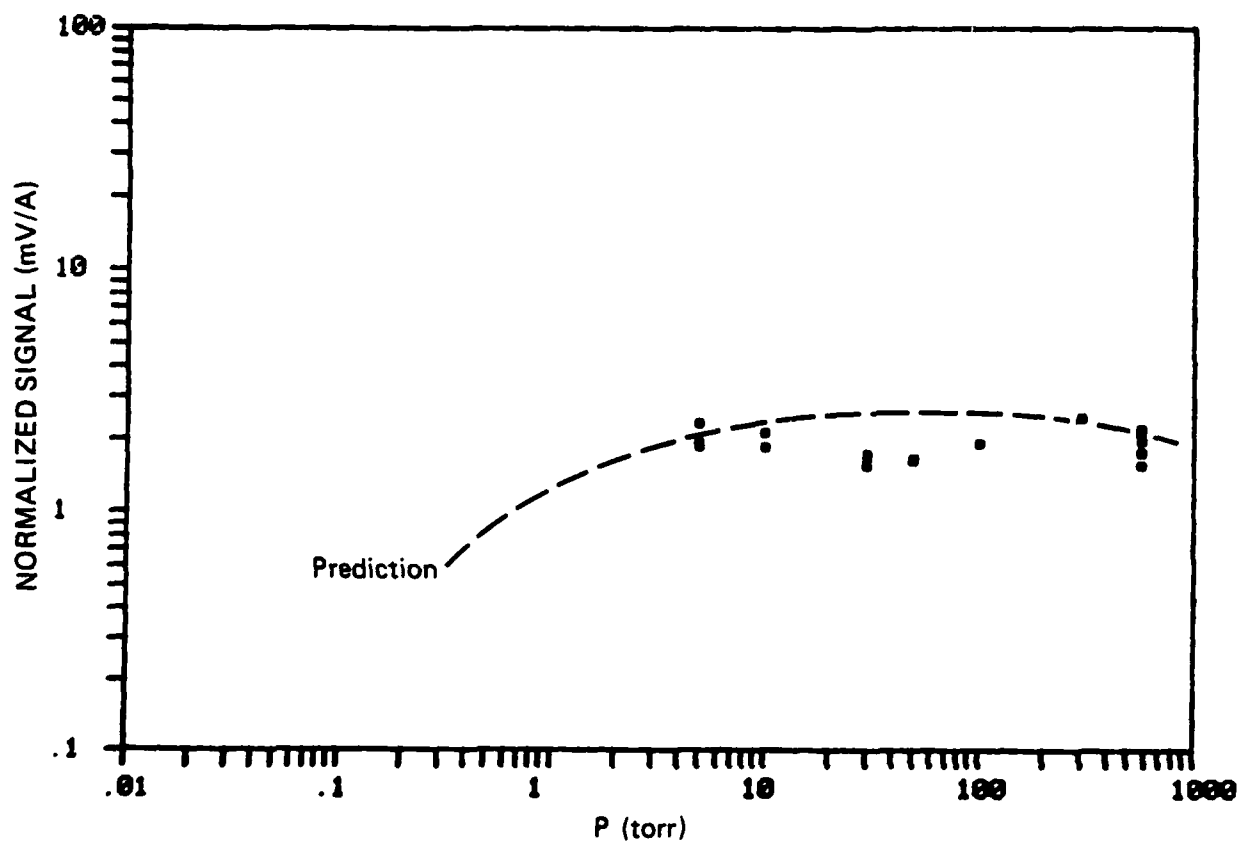
JA-2690-113

FIGURE 14 NORMALIZED 391.4-nm SIGNALS VERSUS PRESSURE
FOR MICROPULSE No. 2



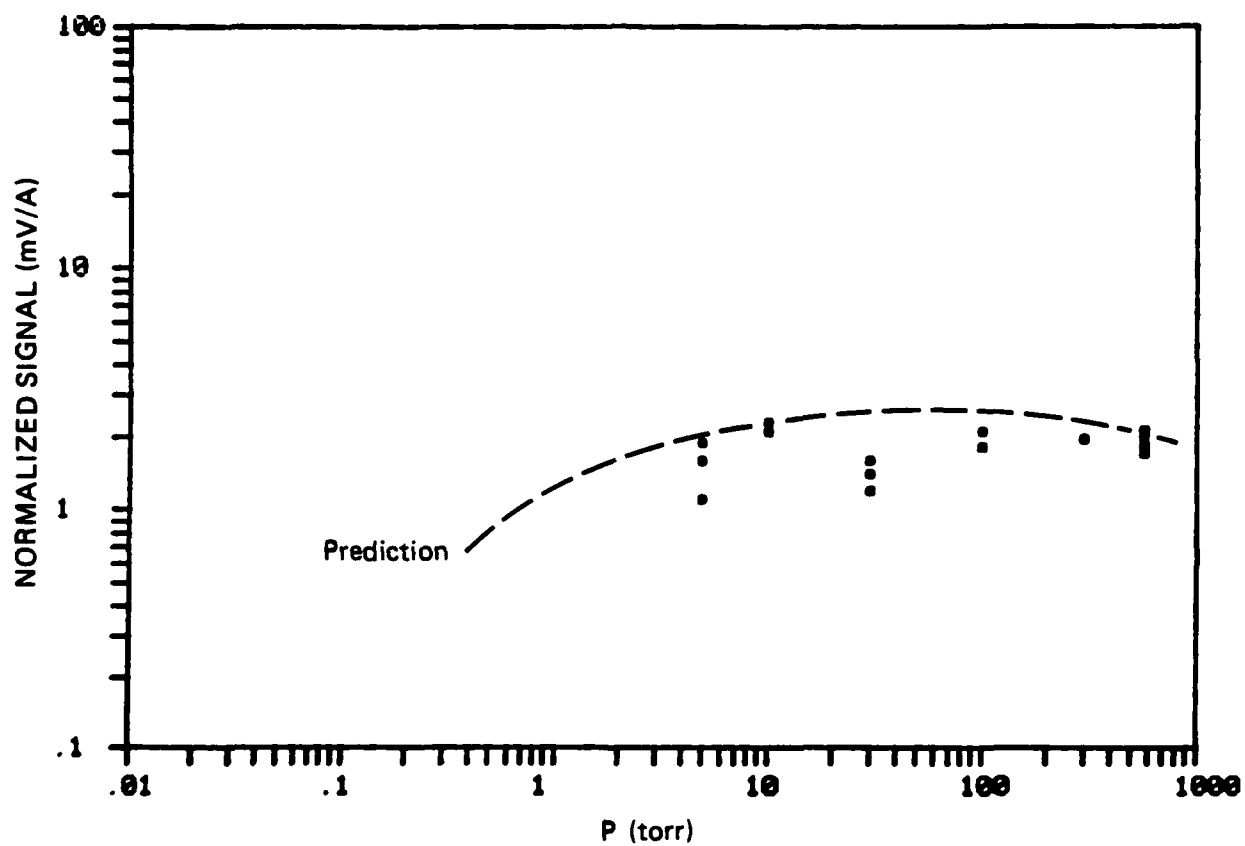
JA-2690-114

FIGURE 15 NORMALIZED 391.4-nm SIGNALS VERSUS PRESSURE
FOR MICROPULSE No. 3



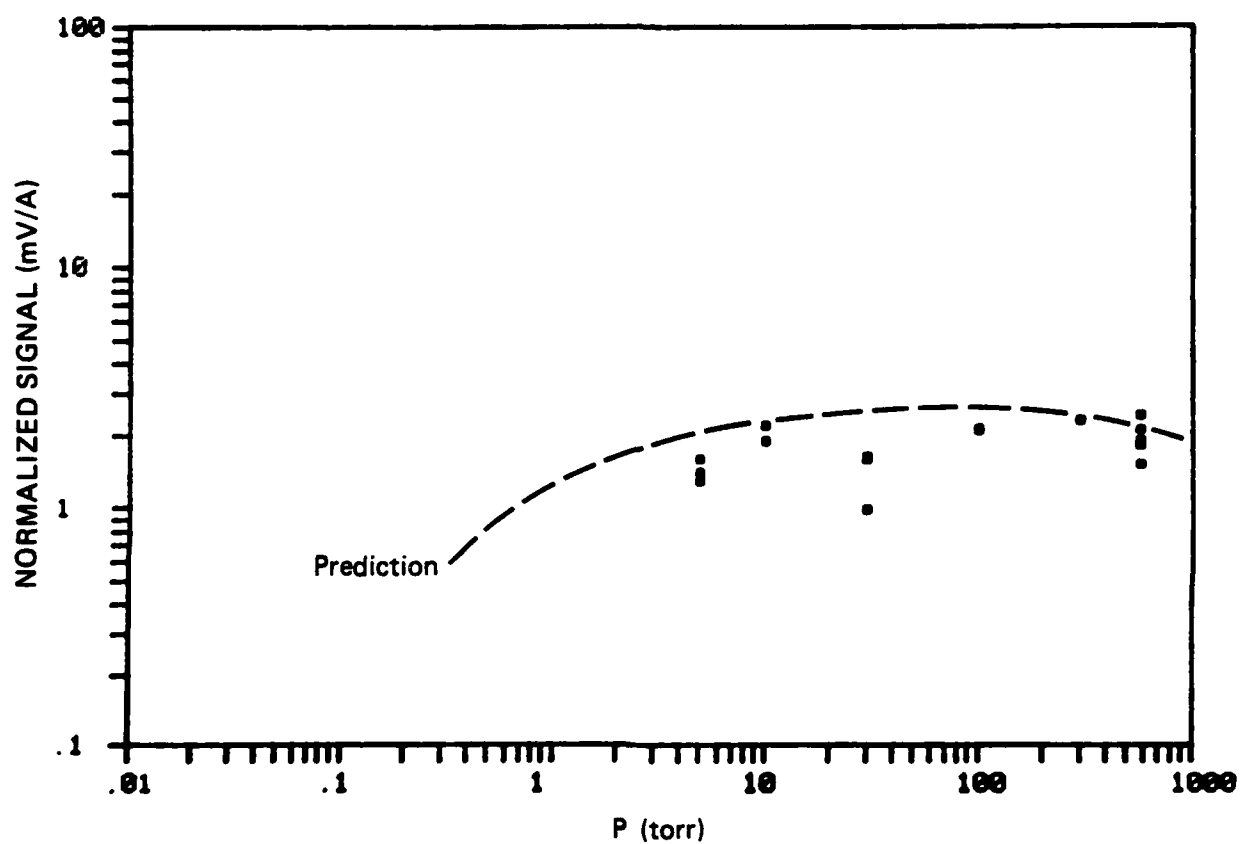
JA-2690-115

FIGURE 16 NORMALIZED 391.4-nm SIGNALS VERSUS PRESSURE
FOR MICROPULSE No. 4



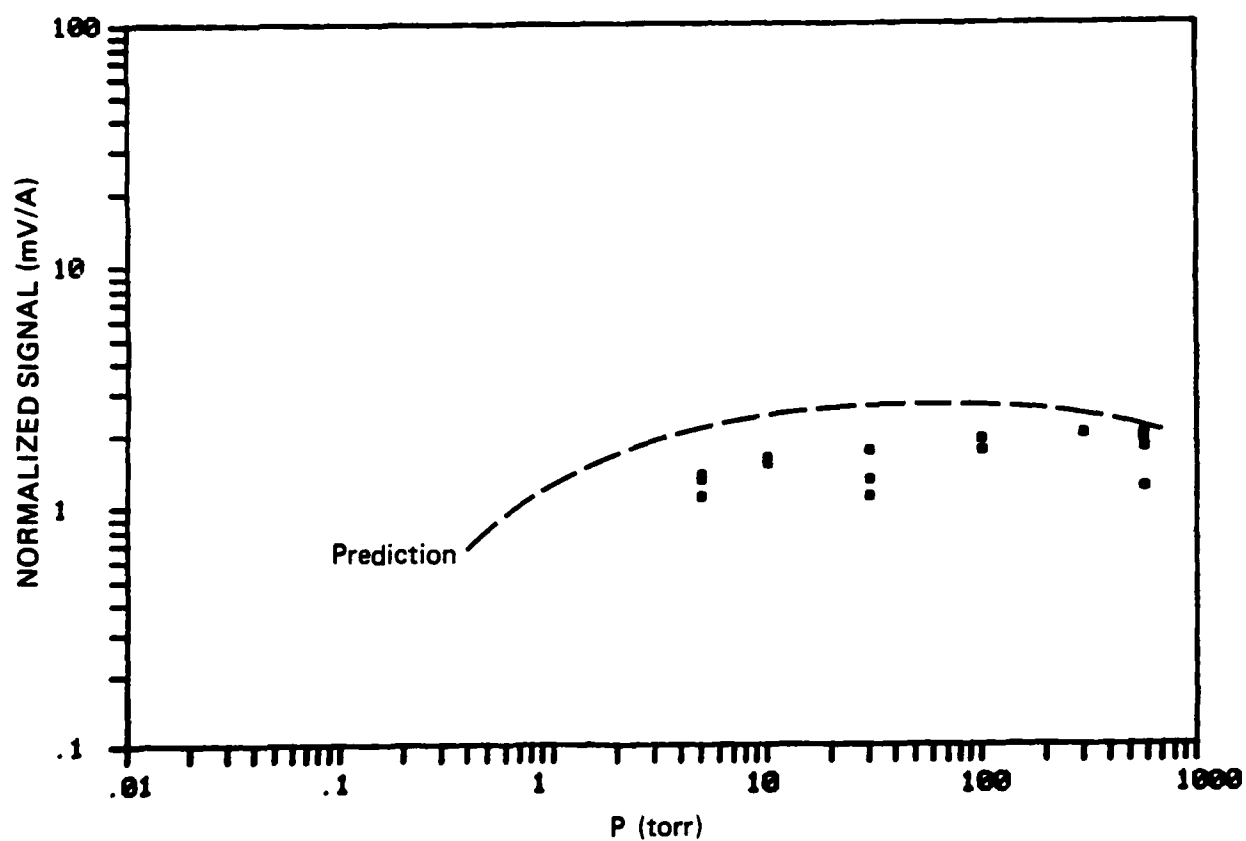
JA-2690-116

FIGURE 17 NORMALIZED 391.4-nm SIGNALS VERSUS PRESSURE
FOR MICROPULSE No. 5



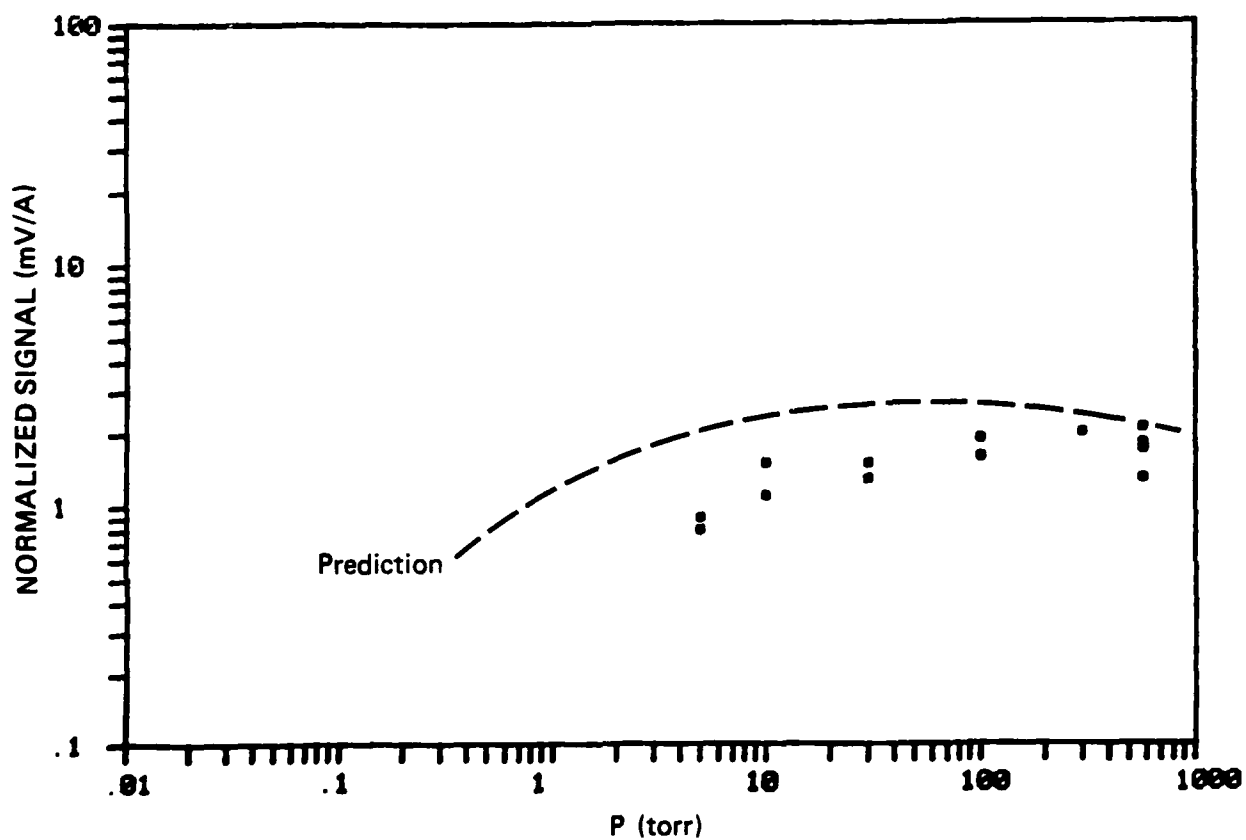
JA-2690-117

FIGURE 18 NORMALIZED 391.4-nm SIGNALS VERSUS PRESSURE
FOR MICROPULSE No. 6



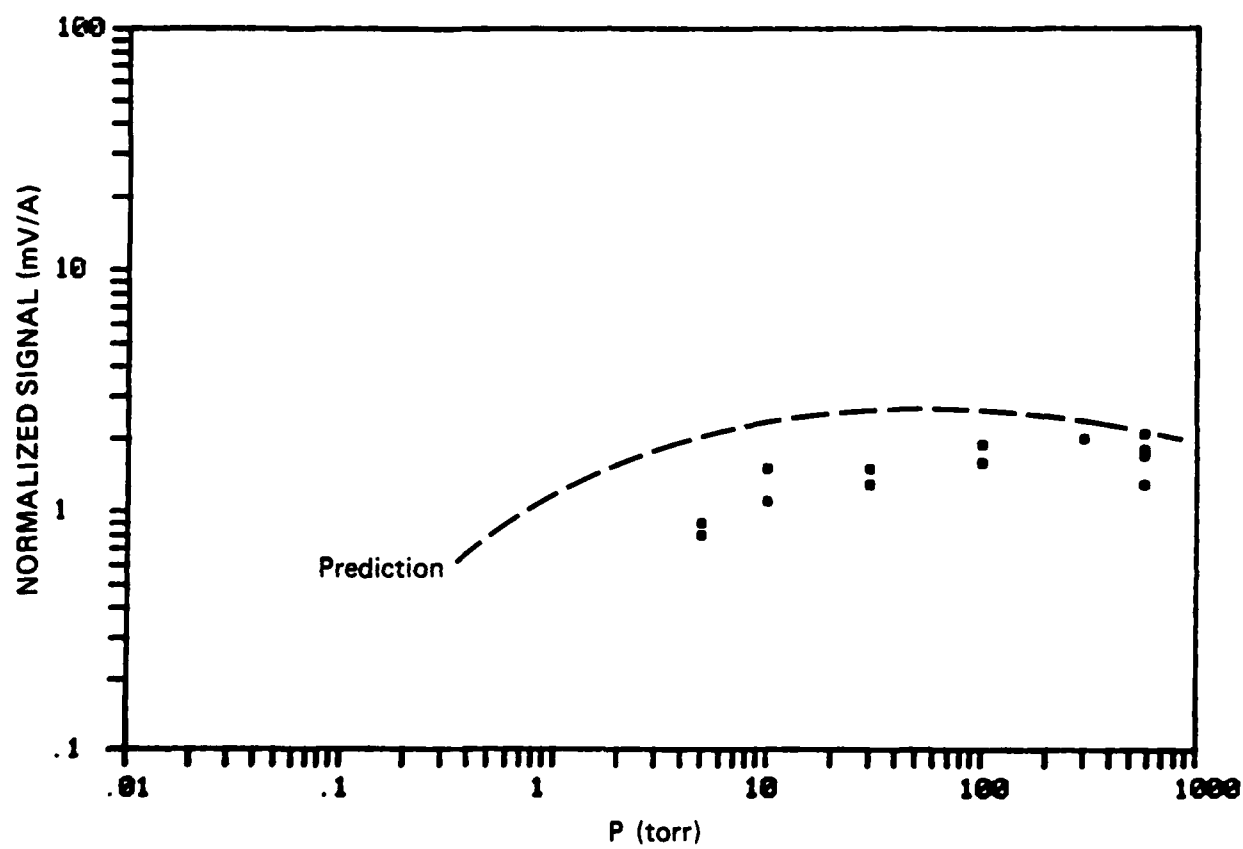
JA-2690-118

FIGURE 19 NORMALIZED 391.4-nm SIGNALS VERSUS PRESSURE
FOR MICROPULSE No. 7



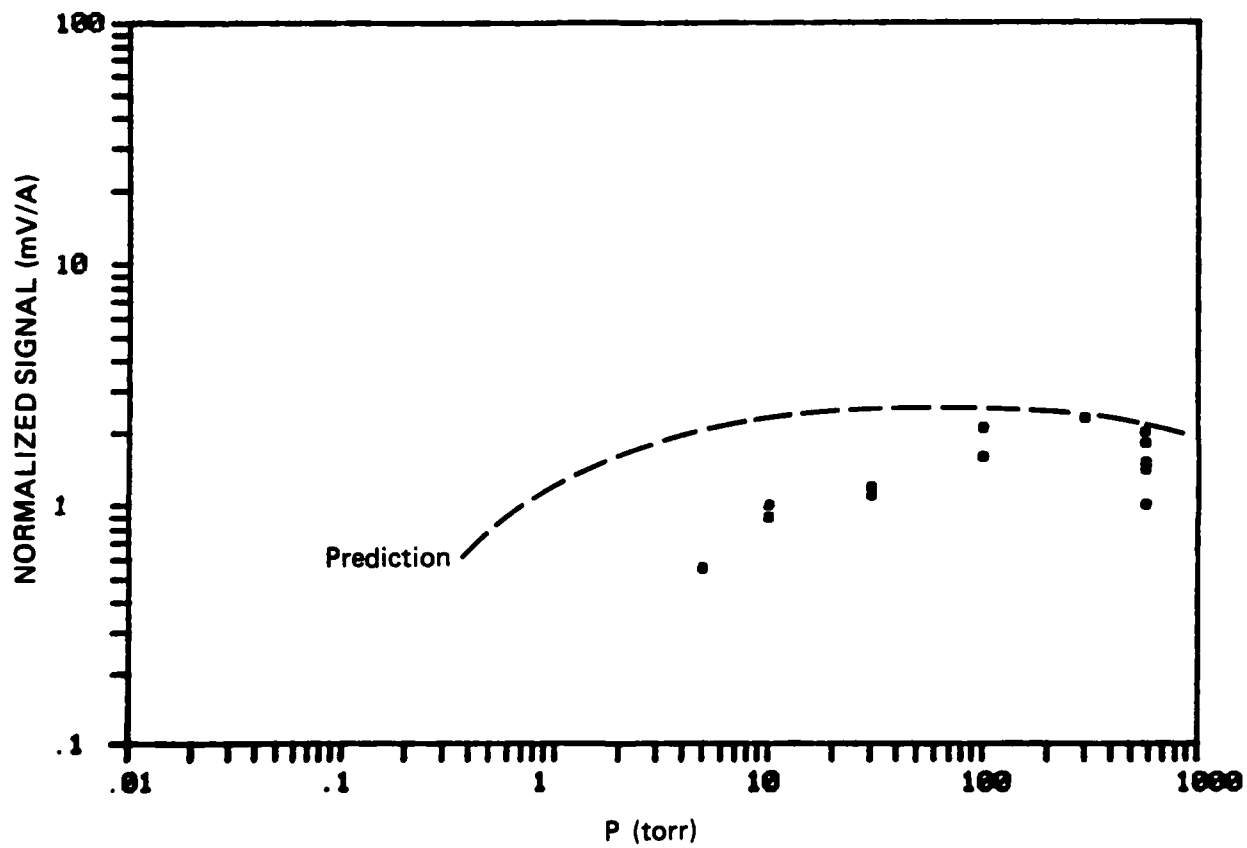
JA-2690-119

FIGURE 20 NORMALIZED 391.4-nm SIGNALS VERSUS PRESSURE
FOR MICROPULSE No. 8



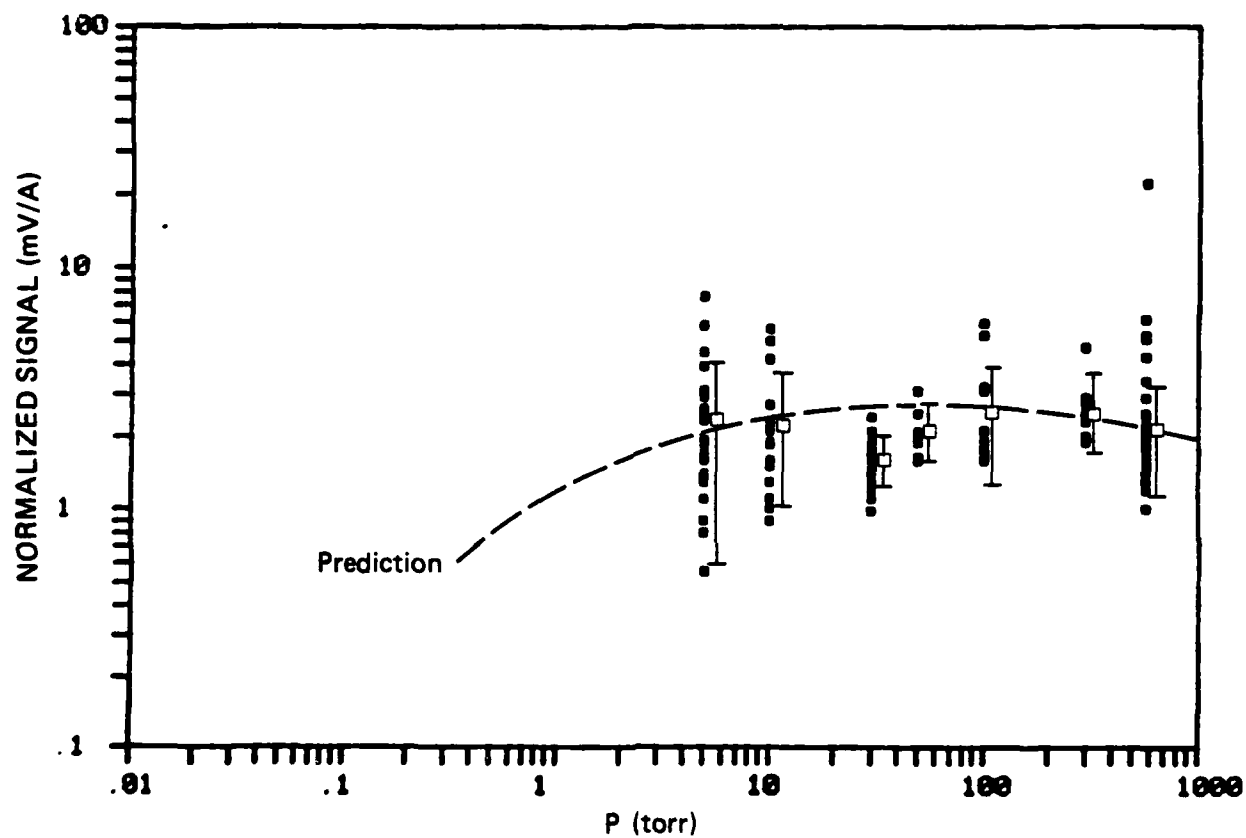
JA-2690-119

FIGURE 20 NORMALIZED 391.4-nm SIGNALS VERSUS PRESSURE
FOR MICROPULSE No. 8



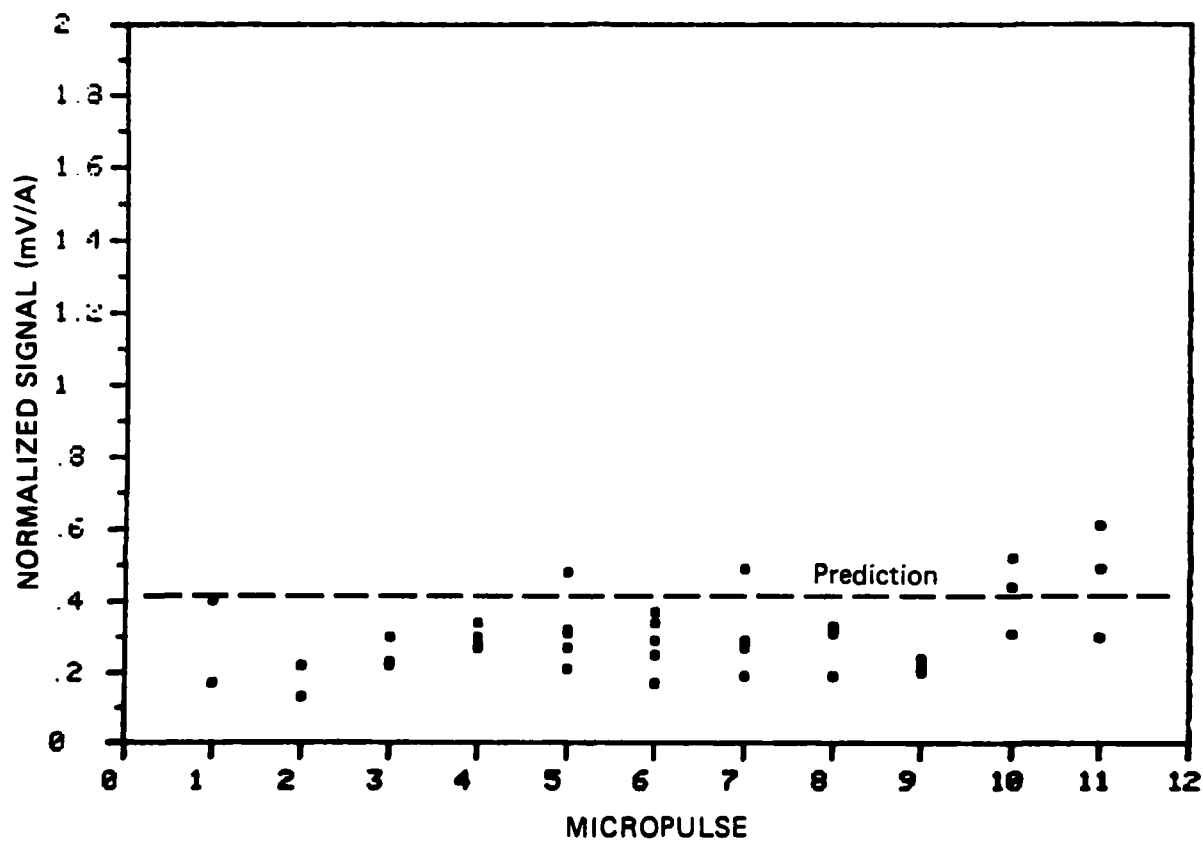
JA-2690-120

FIGURE 21 NORMALIZED 391.4-nm SIGNALS VERSUS PRESSURE
FOR MICROPULSE No. 9



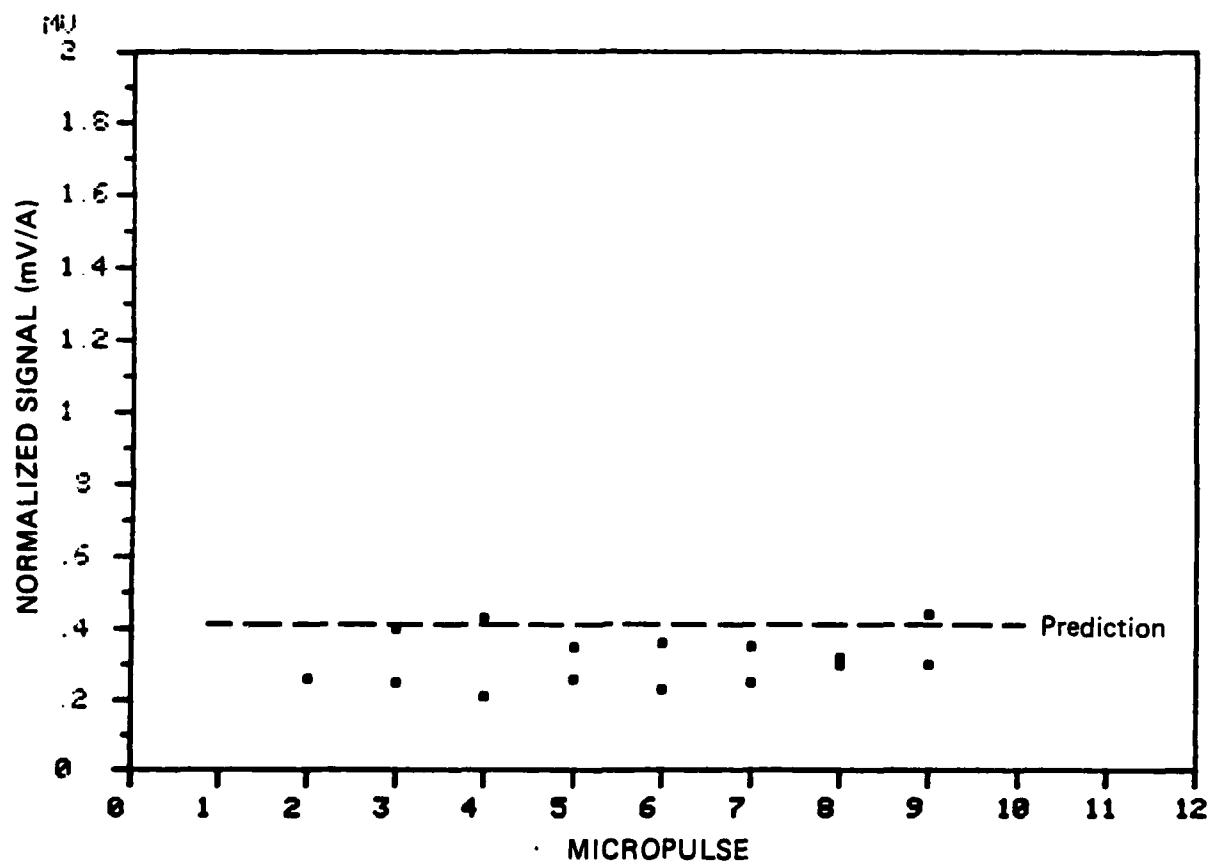
JA-2690-121

FIGURE 22 SUPERPOSITION OF ALL NORMALIZED 391.4-nm SIGNALS
VERSUS PRESSURE



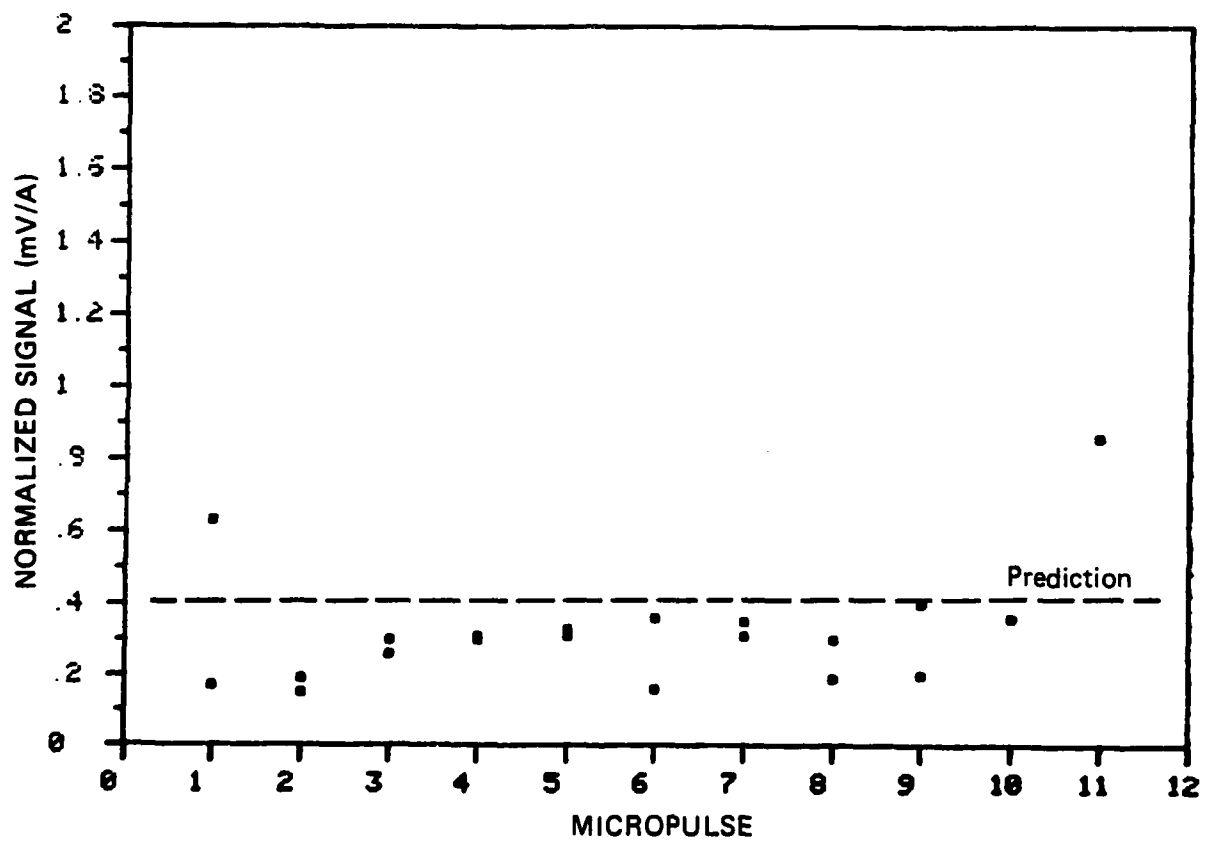
JA-2690-122

FIGURE 23 NORMALIZED 406.0-nm SIGNALS VERSUS MICROPULSE
AT 580 torr



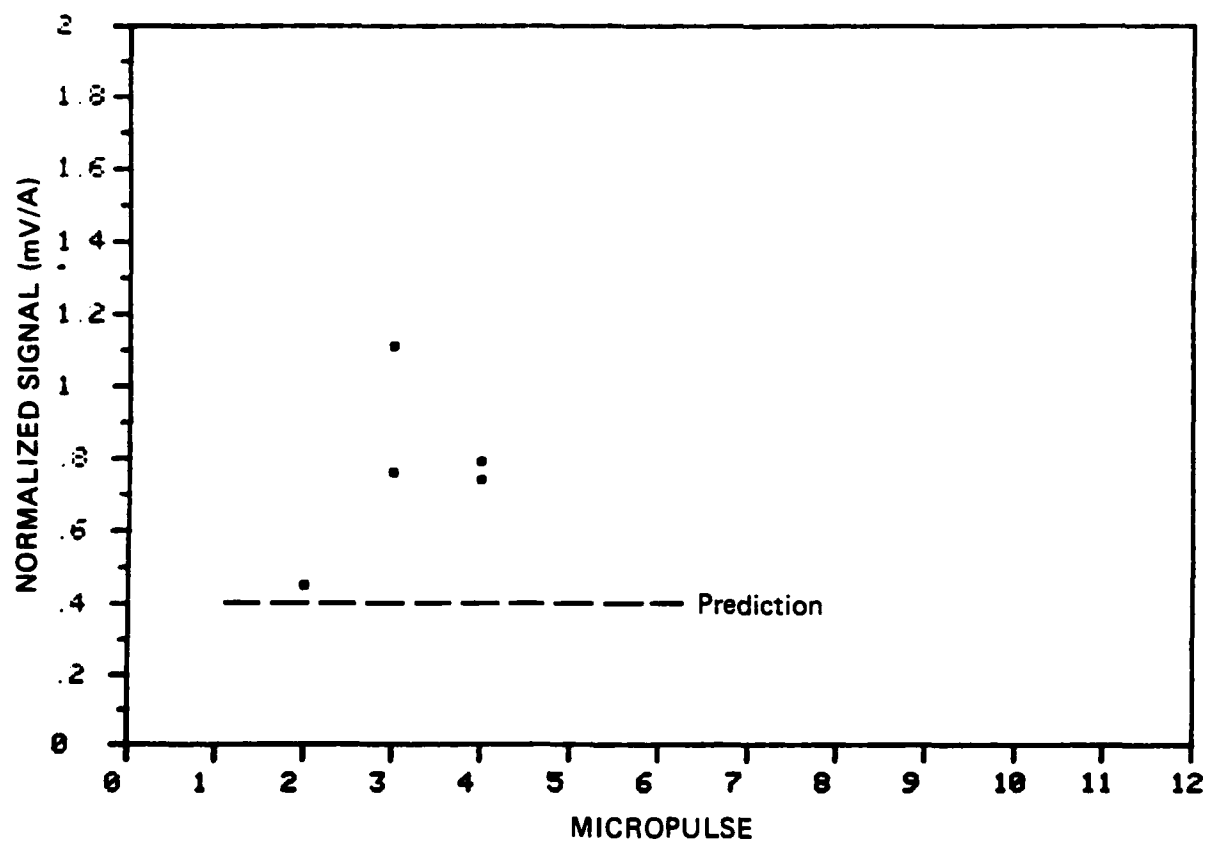
JA-2690-123

FIGURE 24 NORMALIZED 406.0-nm SIGNALS VERSUS MICROPULSE
AT 300 torr



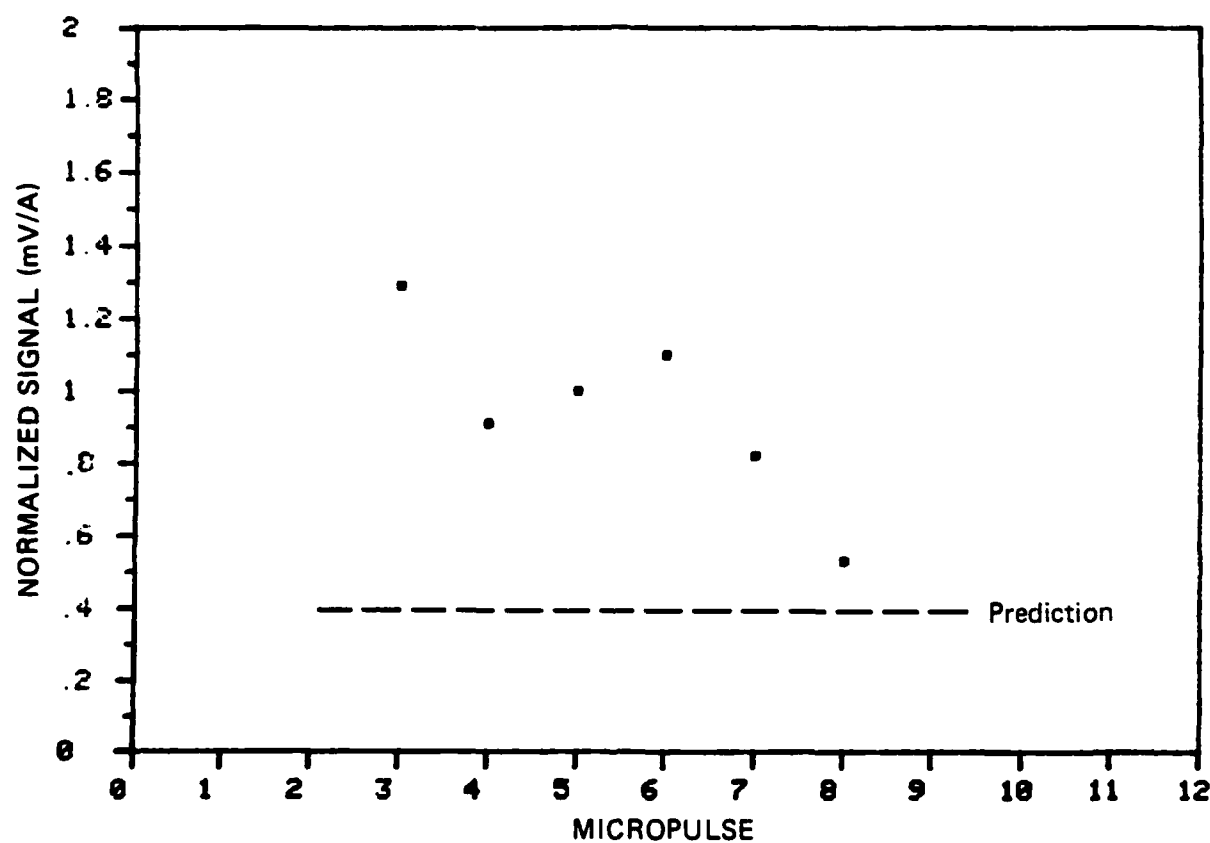
JA-2690-124

FIGURE 25 NORMALIZED 406.0-nm SIGNALS VERSUS MICROPULSE
AT 100 torr



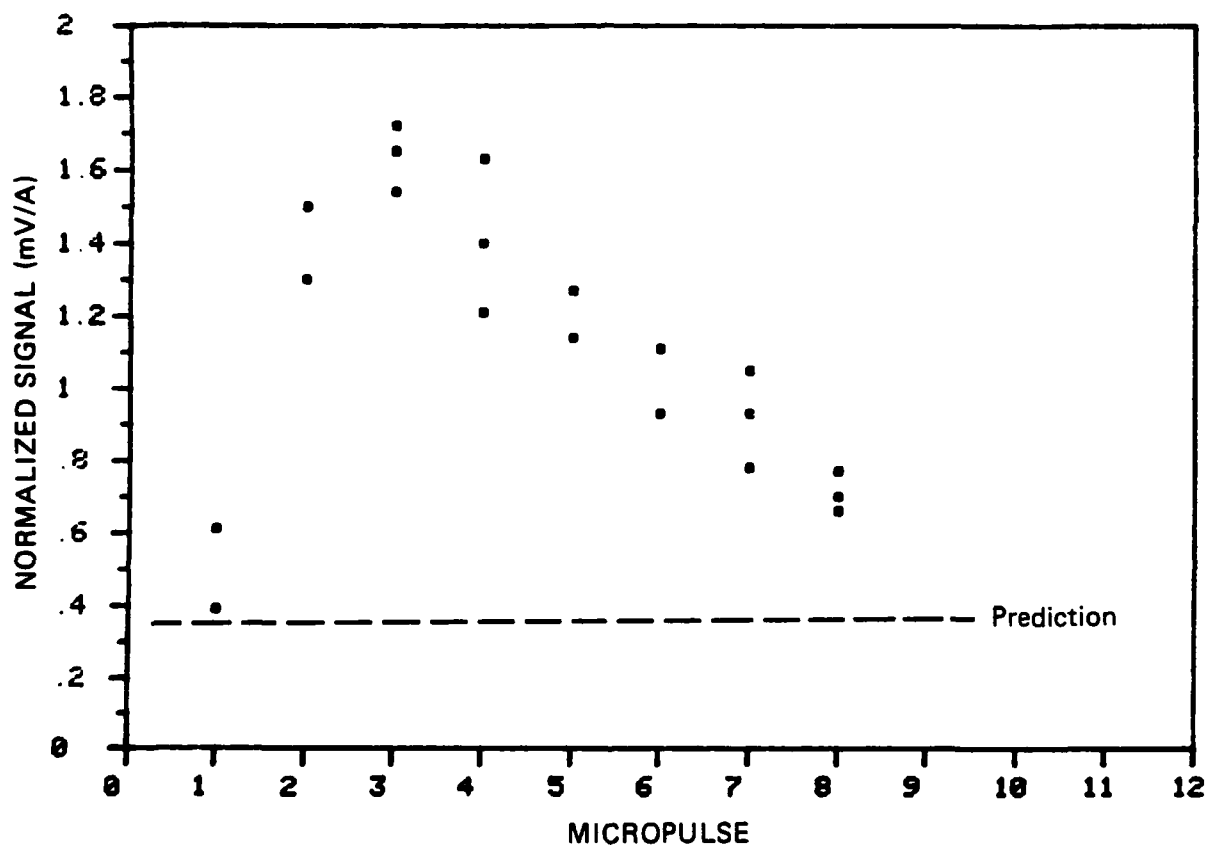
JA-2690-125

FIGURE 26 NORMALIZED 406.0-nm SIGNALS VERSUS MICROPULSE
AT 50 torr



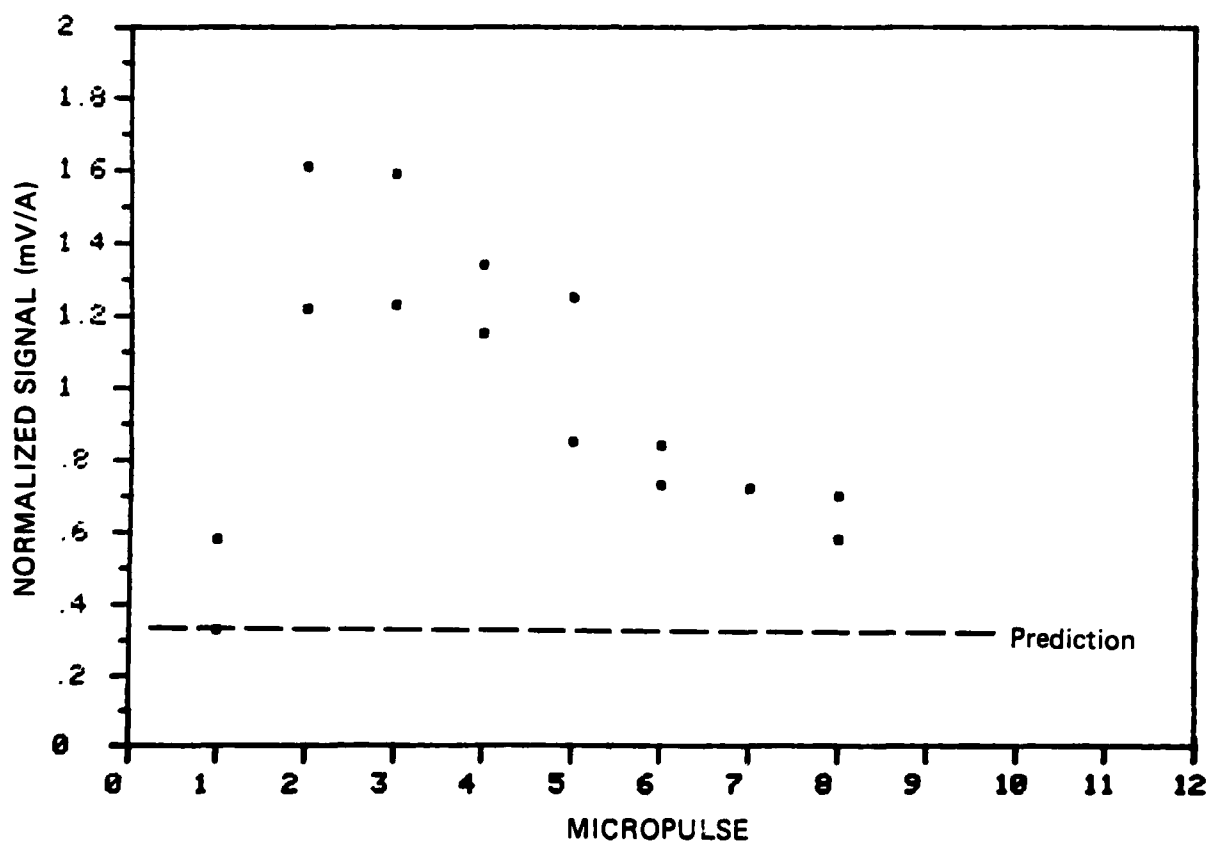
JA-2690-126

FIGURE 27 NORMALIZED 406.0-nm SIGNALS VERSUS MICROPULSE
AT 30 torr



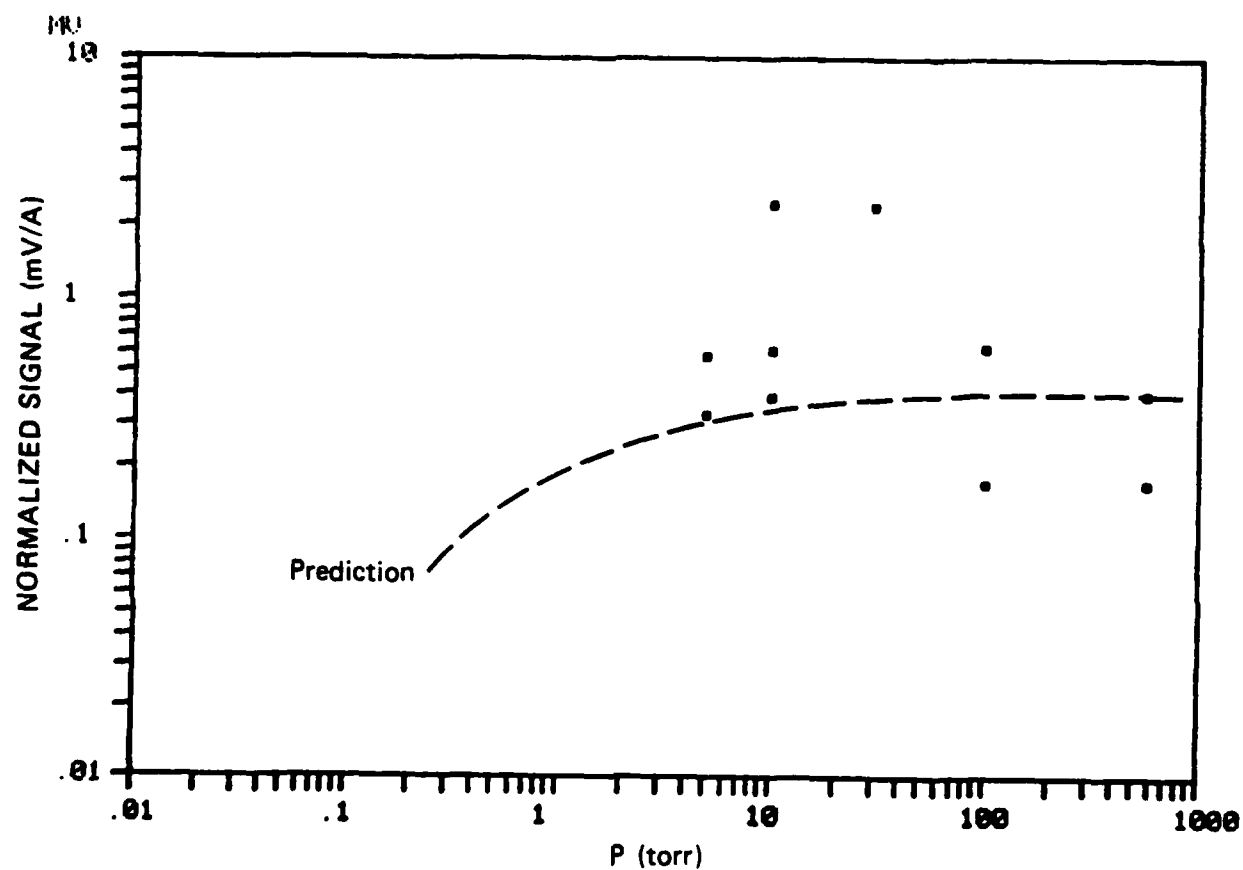
JA-2690-127

FIGURE 28 NORMALIZED 406.0-nm SIGNALS VERSUS MICROPULSE
AT 10 torr



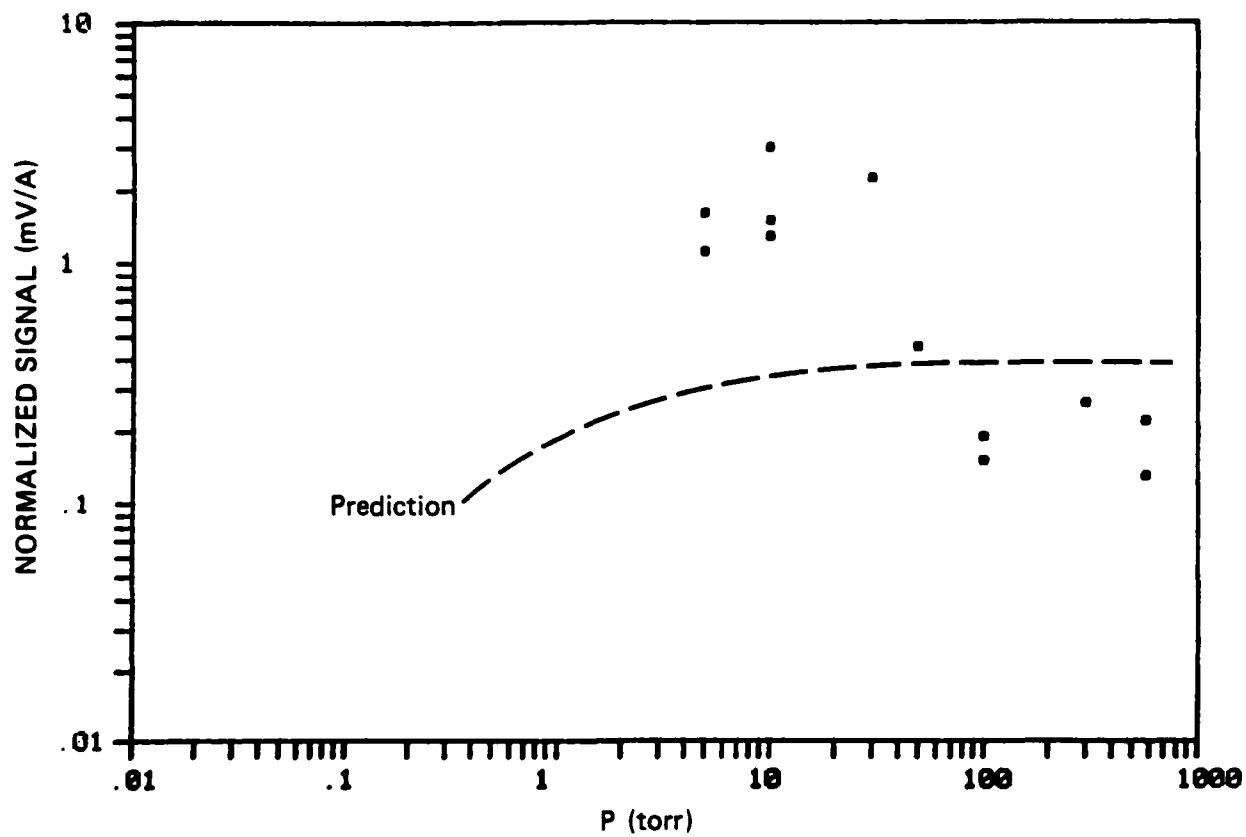
JA-2690-128

FIGURE 29 NORMALIZED 406.9-nm SIGNALS VERSUS MICROPULSE
AT 5 torr



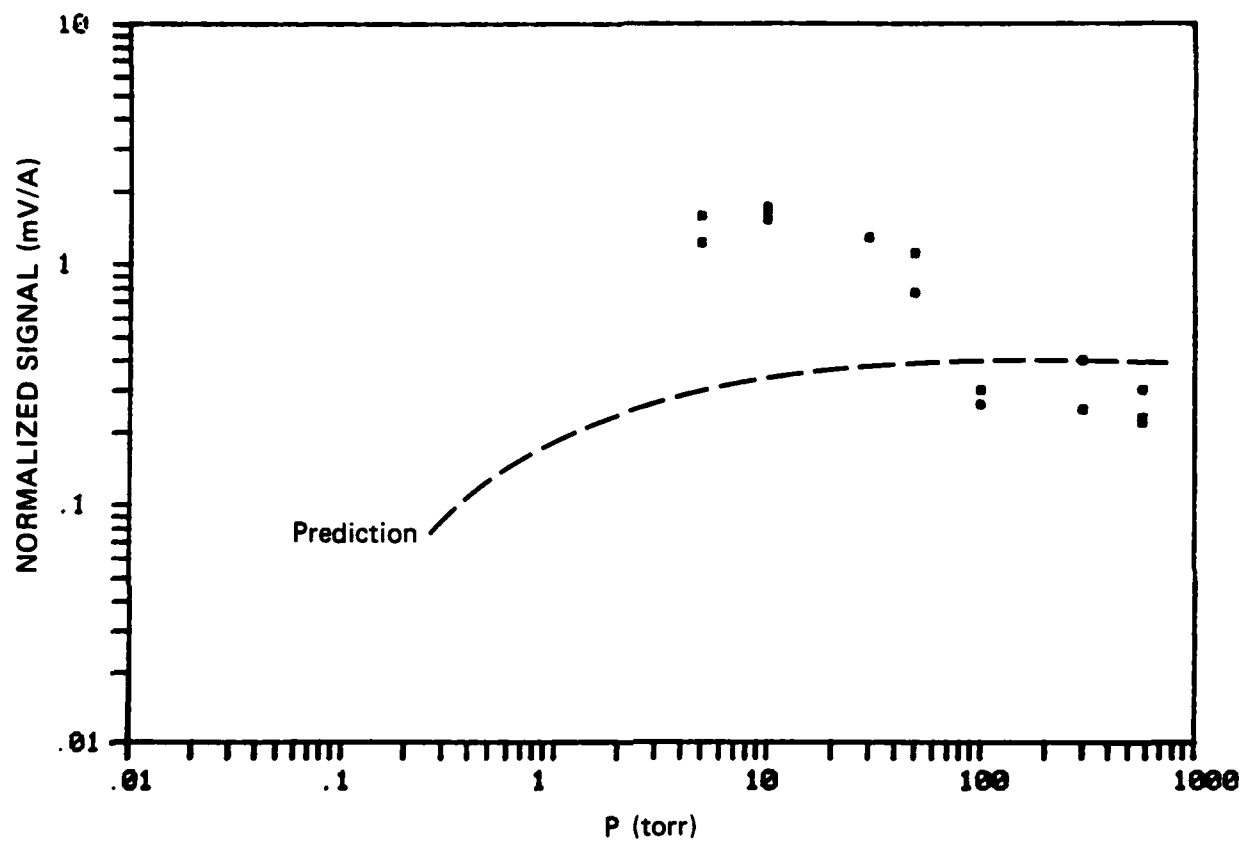
JA-2690-129

FIGURE 30 NORMALIZED 406.0-nm SIGNALS VERSUS PRESSURE
FOR MICROPULSE No. 1



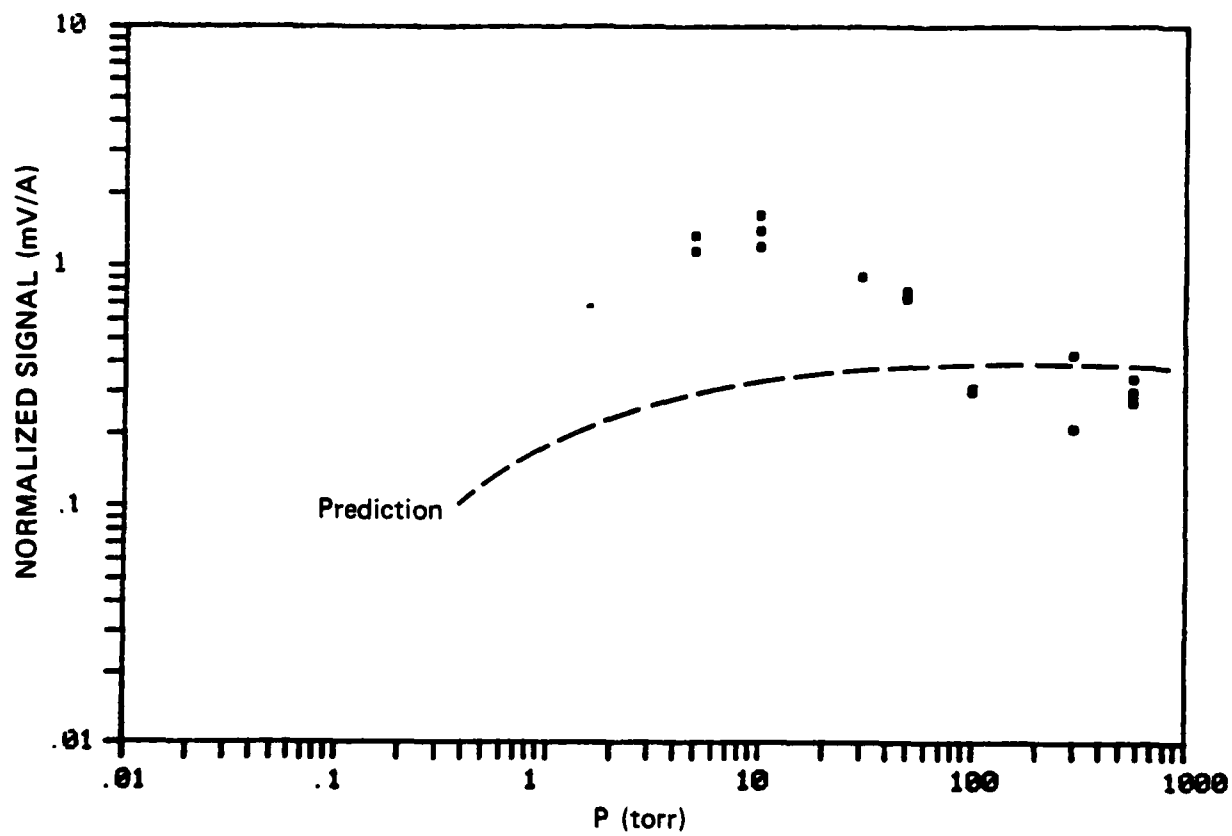
JA-2690-130

FIGURE 31 NORMALIZED 406.0-nm SIGNALS VERSUS PRESSURE
FOR MICROPULSE No. 2



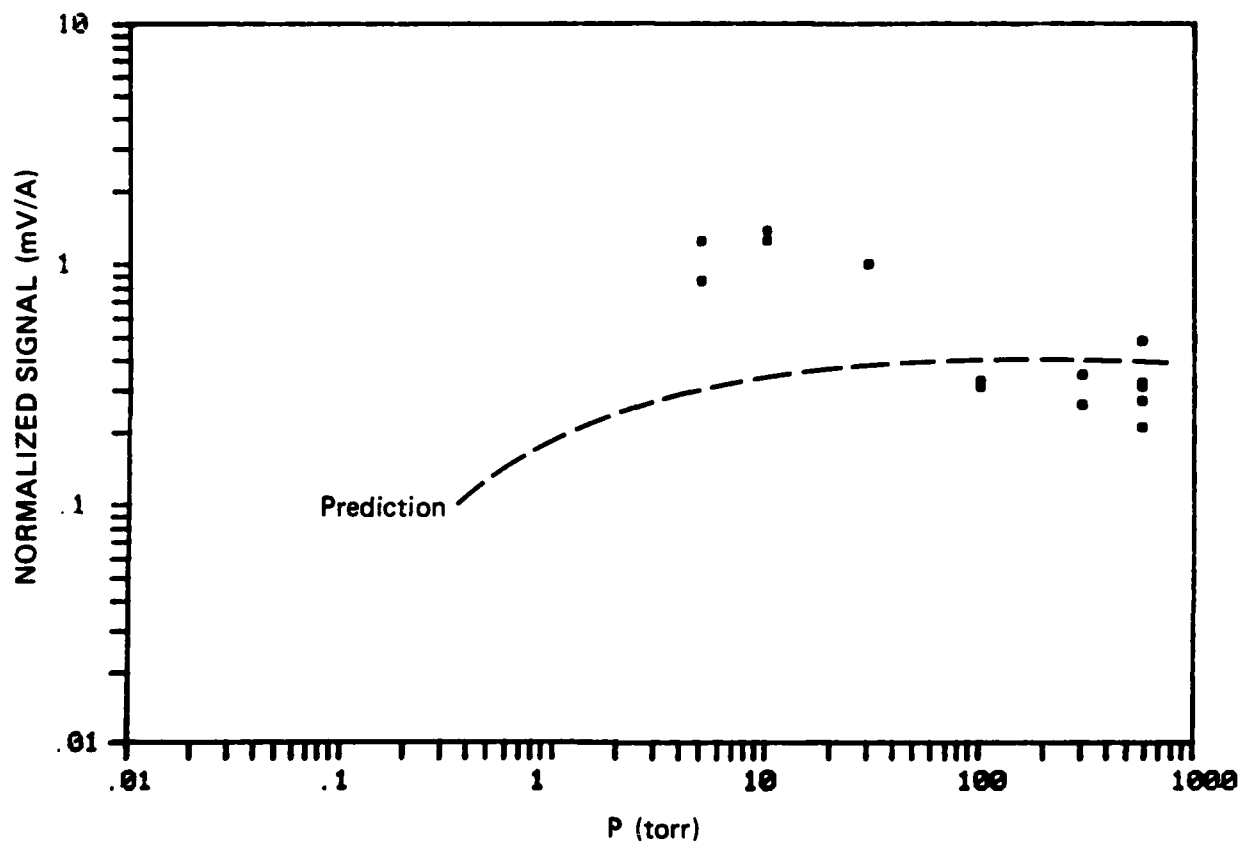
JA-2690-131

FIGURE 32 NORMALIZED 406.0-nm SIGNALS VERSUS PRESSURE
FOR MICROPULSE No. 3



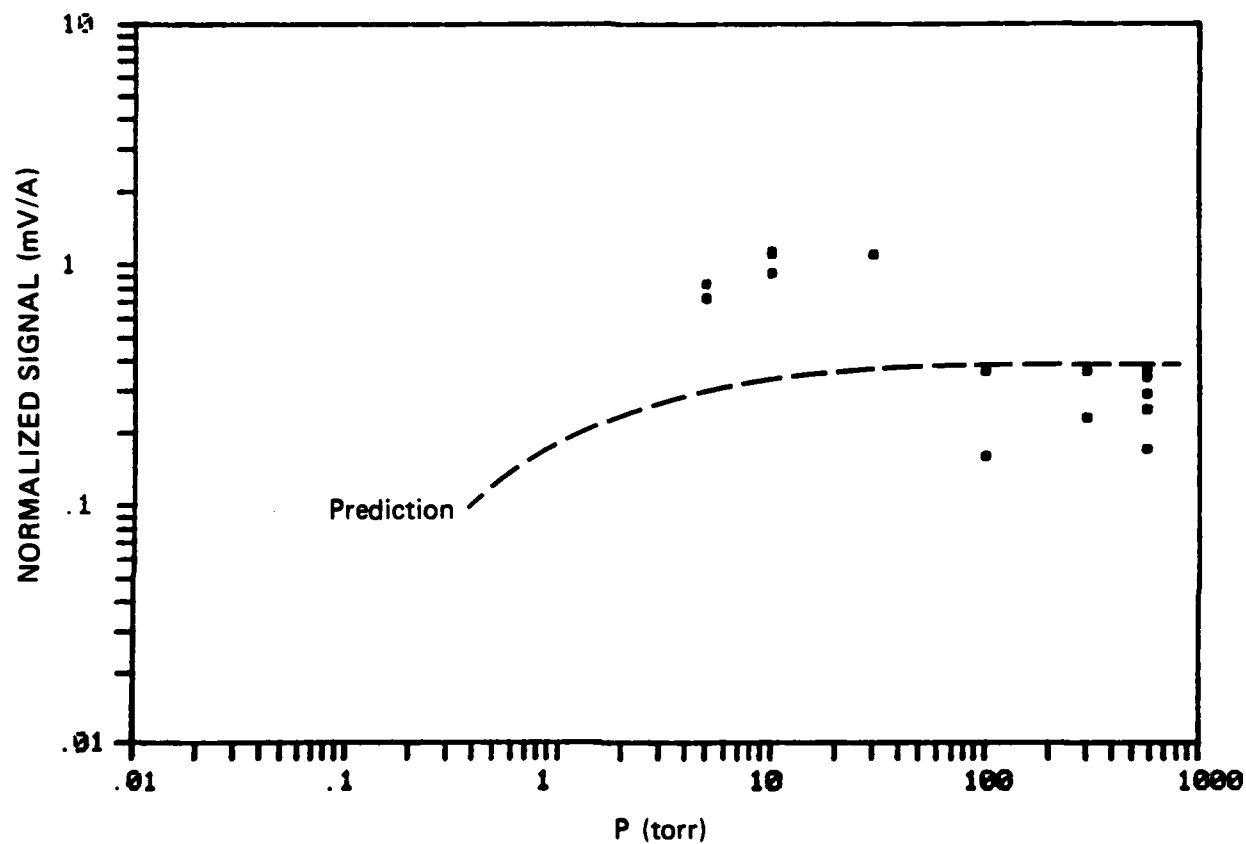
JA-2690-132

FIGURE 33 NORMALIZED 406.0-nm SIGNALS VERSUS PRESSURE
FOR MICROPULSE No. 4



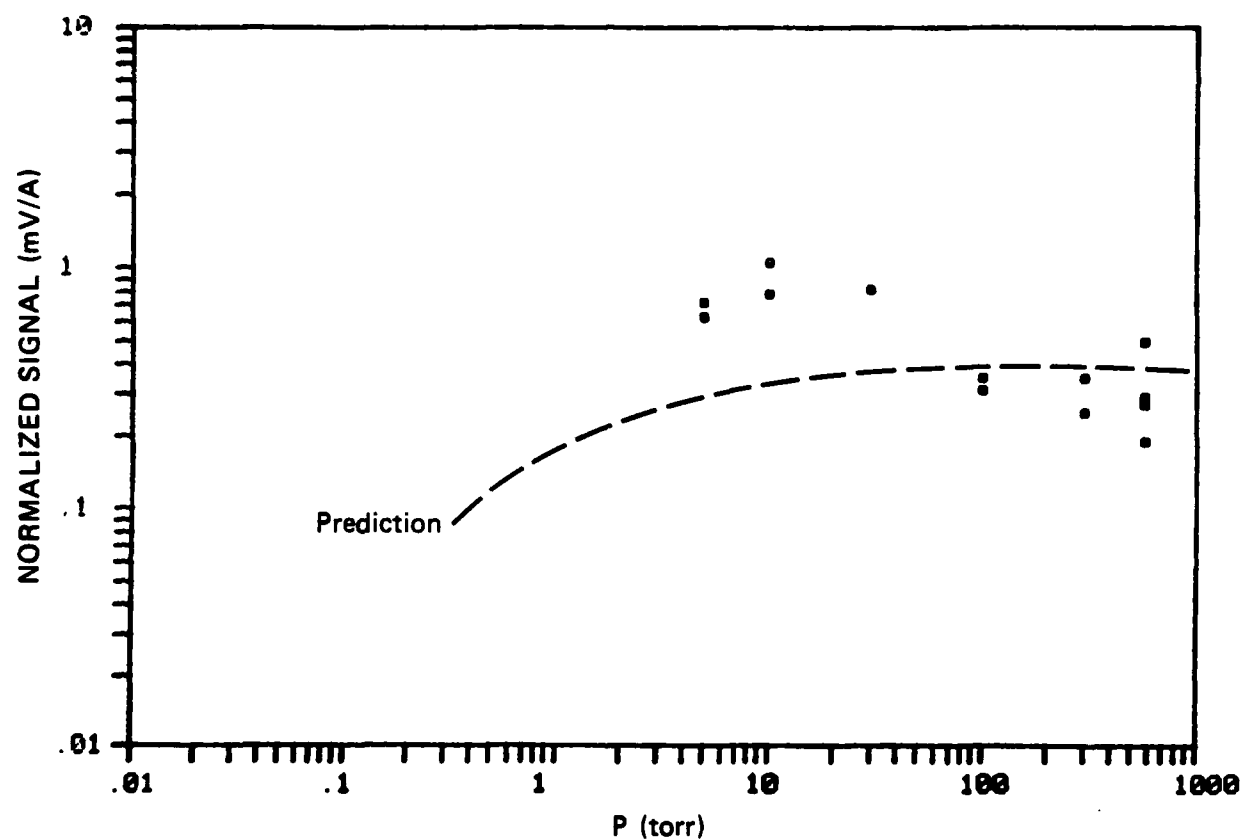
JA-2690-133

FIGURE 34 NORMALIZED 406.0-nm SIGNALS VERSUS PRESSURE
FOR MICROPULSE No. 5



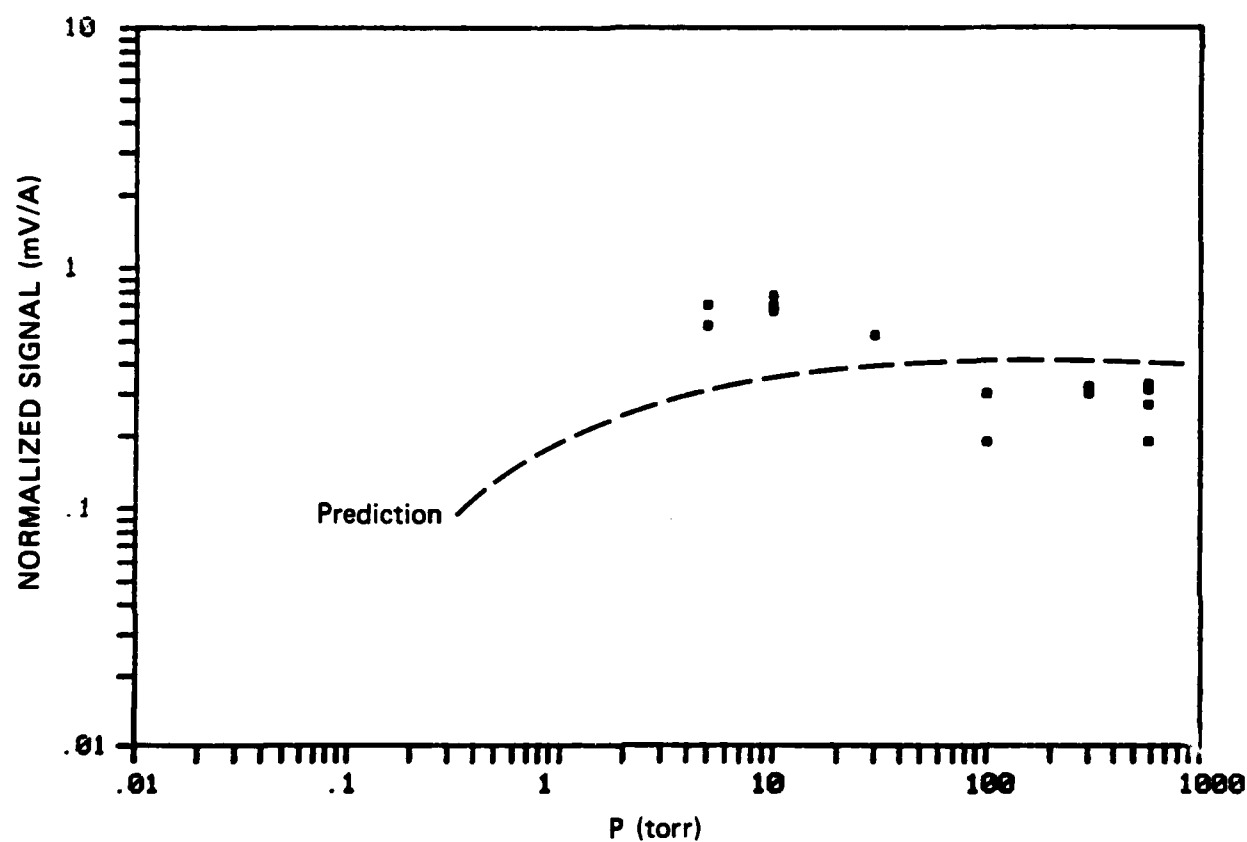
JA-2690-134

FIGURE 35 NORMALIZED 406.0-nm SIGNALS VERSUS PRESSURE
FOR MICROPULSE No. 6



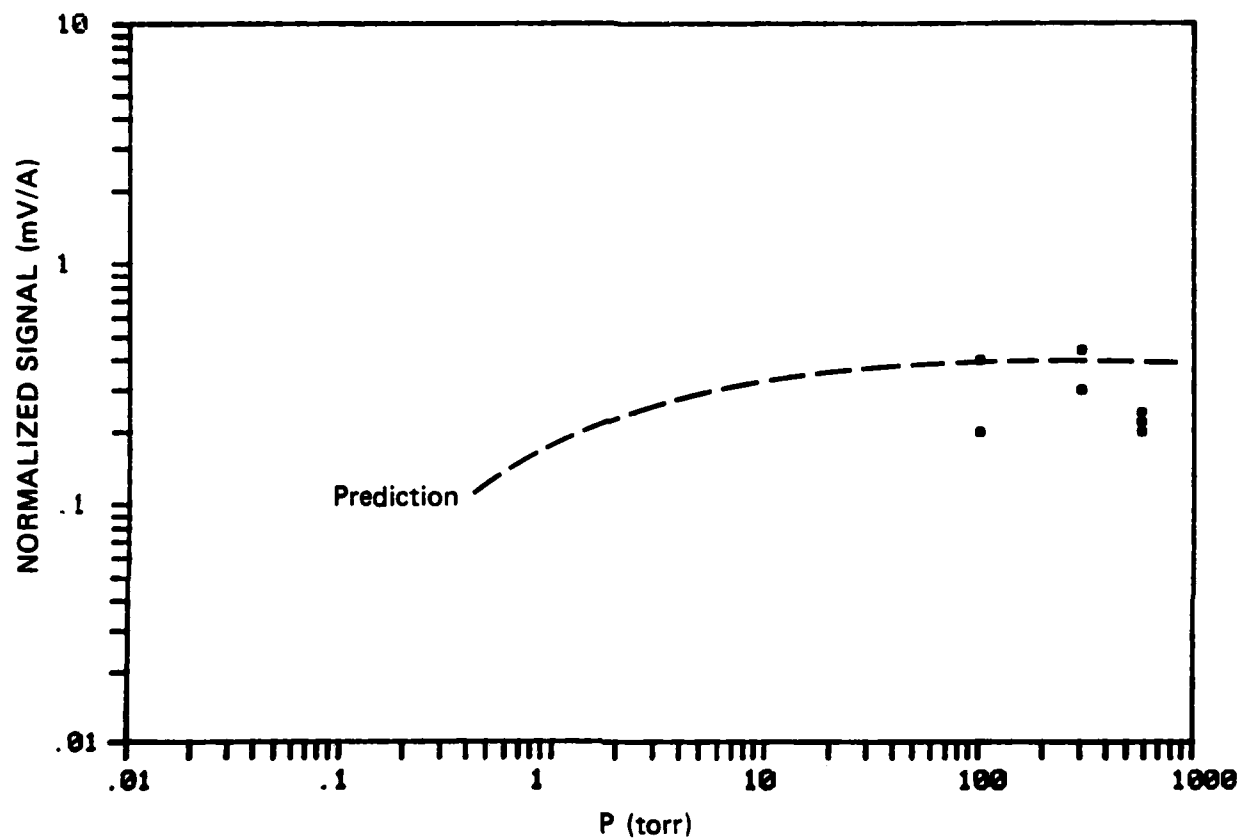
JA-2690-135

FIGURE 36 NORMALIZED 406.0-nm SIGNALS VERSUS PRESSURE
FOR MICROPULSE No. 7



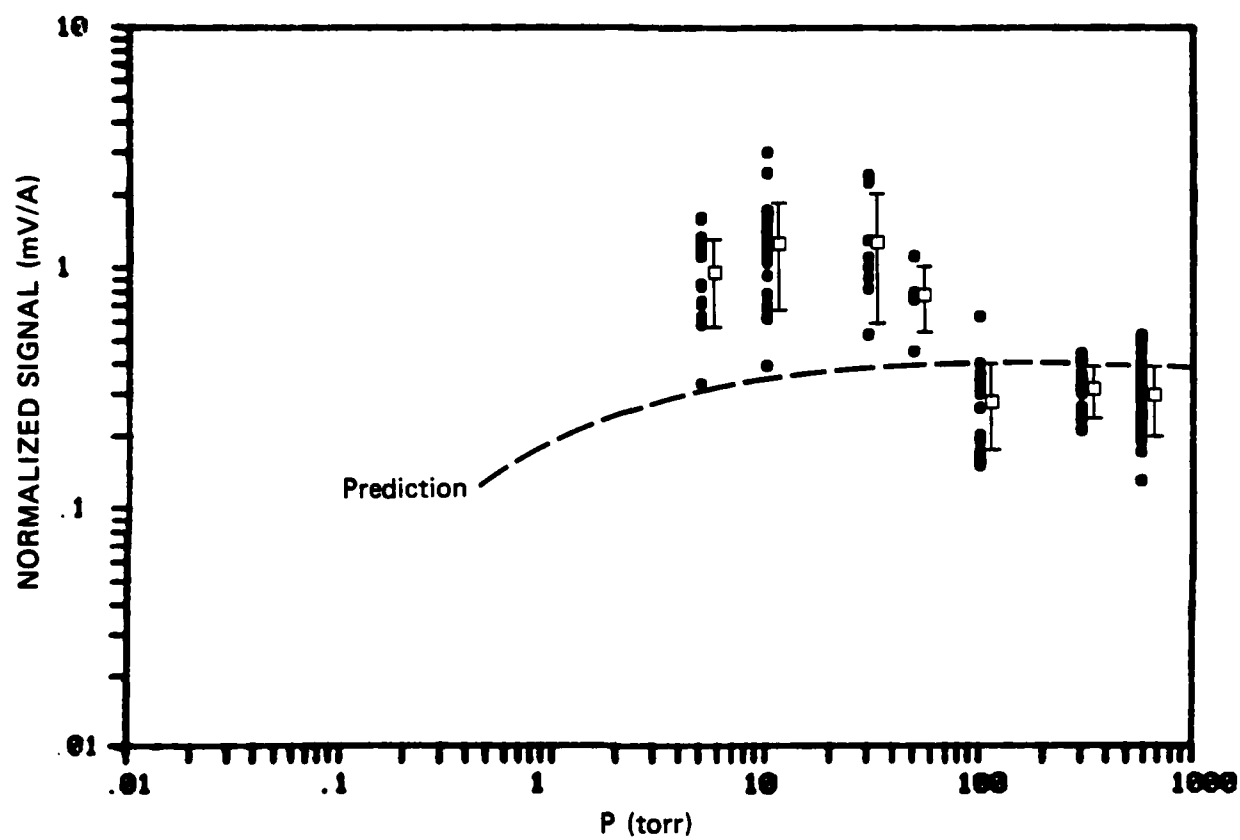
JA-2690-136

FIGURE 37 NORMALIZED 406.0-nm SIGNALS VERSUS PRESSURE
FOR MICROPULSE No. 8



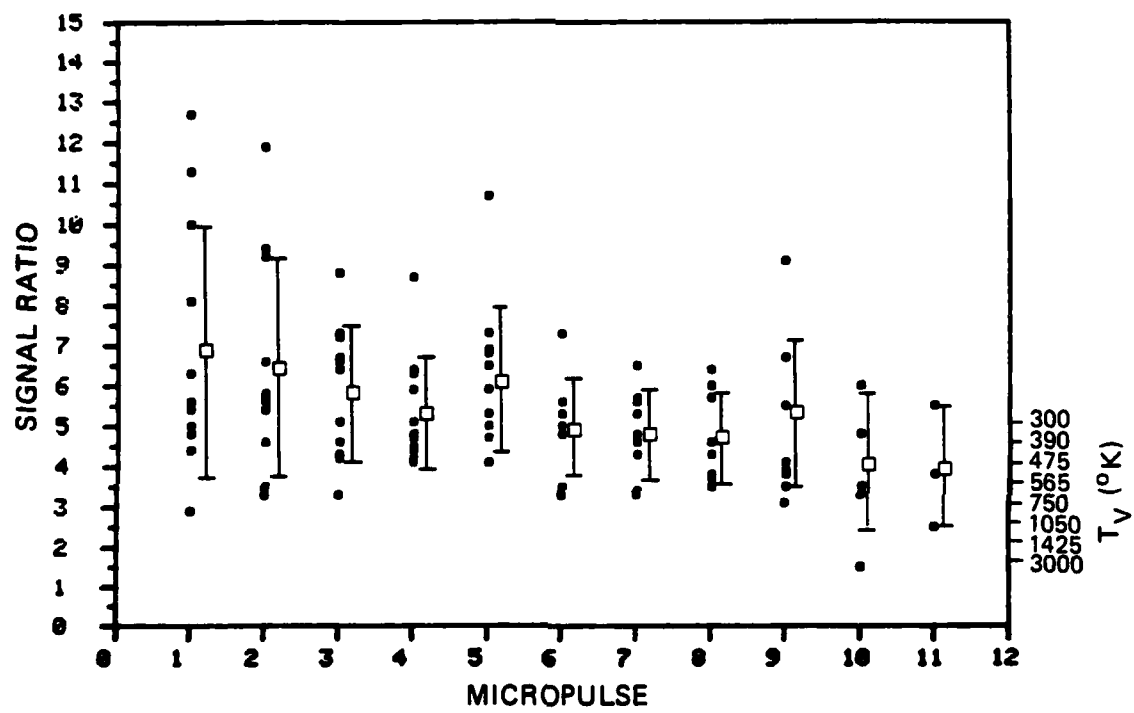
JA-2690-137

FIGURE 38 NORMALIZED 406.0-nm SIGNALS VERSUS PRESSURE
FOR MICROPULSE No. 9



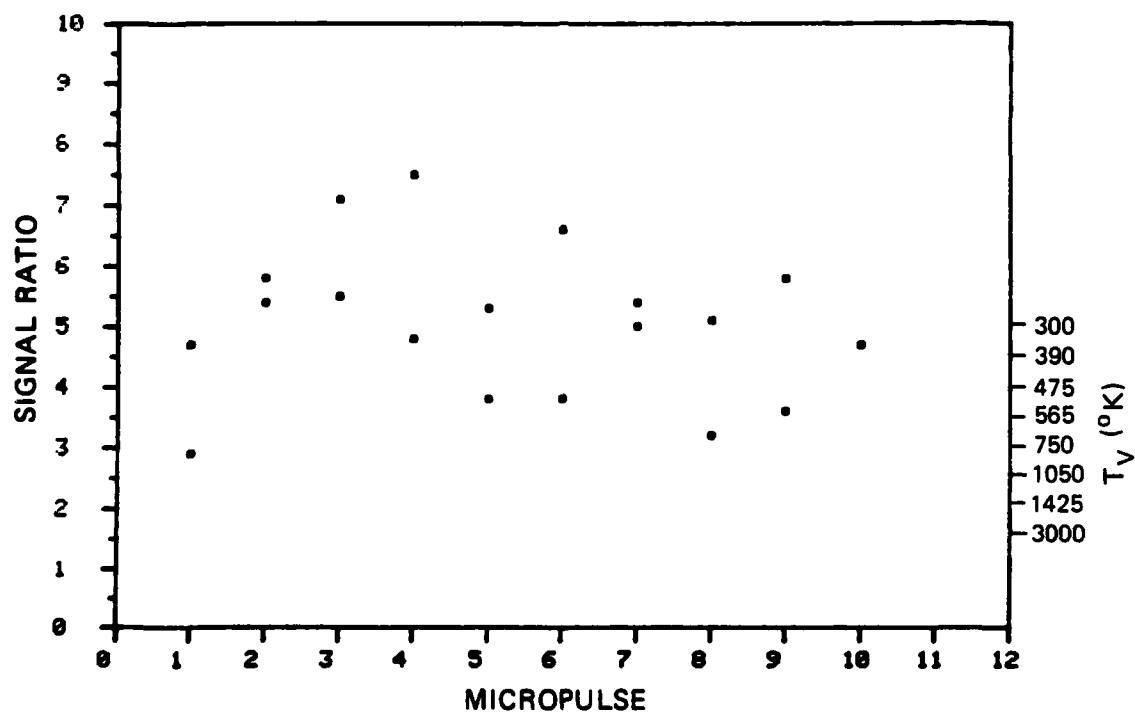
JA-2690-138

FIGURE 39 SUPERPOSITION OF ALL 406.0-nm SIGNALS VERSUS PRESSURE



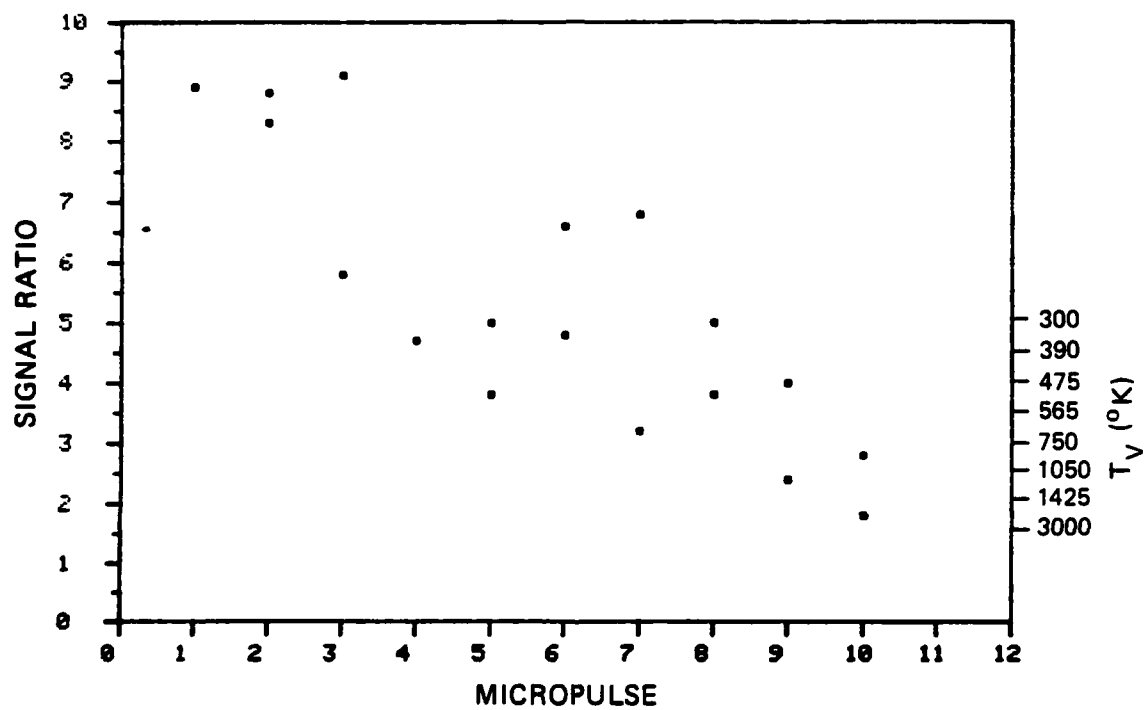
JA-2690-139

FIGURE 40 RATIOS OF 391.4-nm/423.6-nm SIGNALS VERSUS MICROPULSE
AT 580 torr



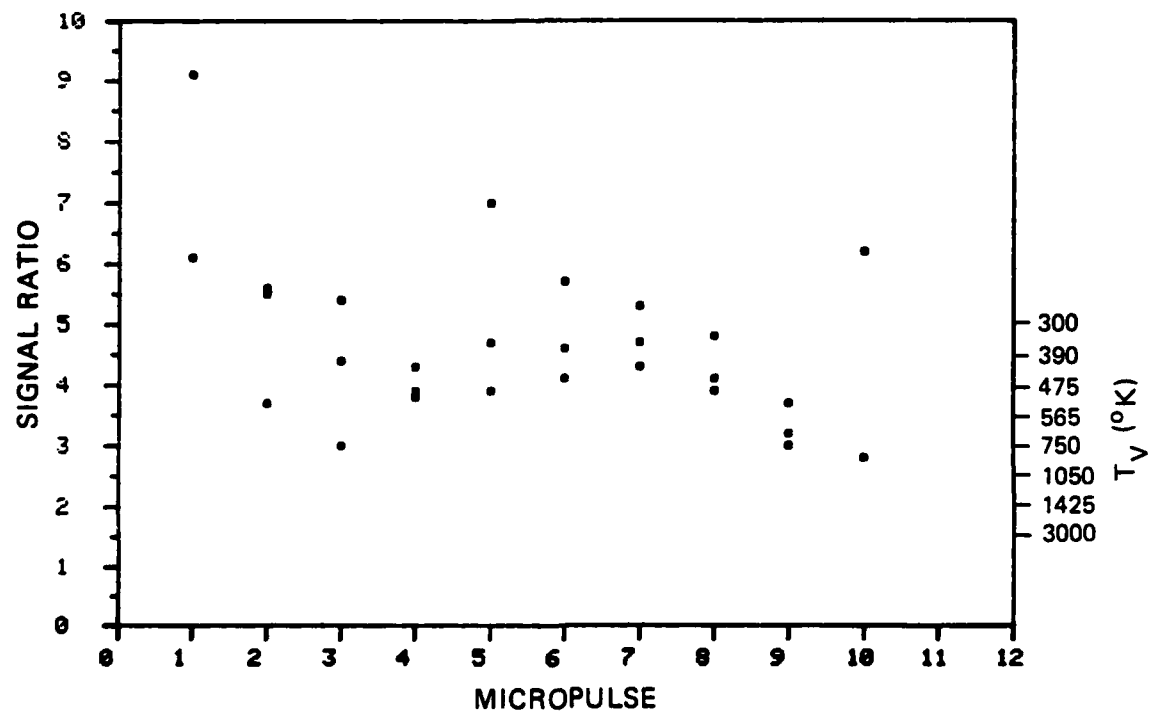
JA-2690-140

FIGURE 41 RATIOS OF 391.4-nm/423.6-nm SIGNALS VERSUS MICROPULSE
AT 300 torr



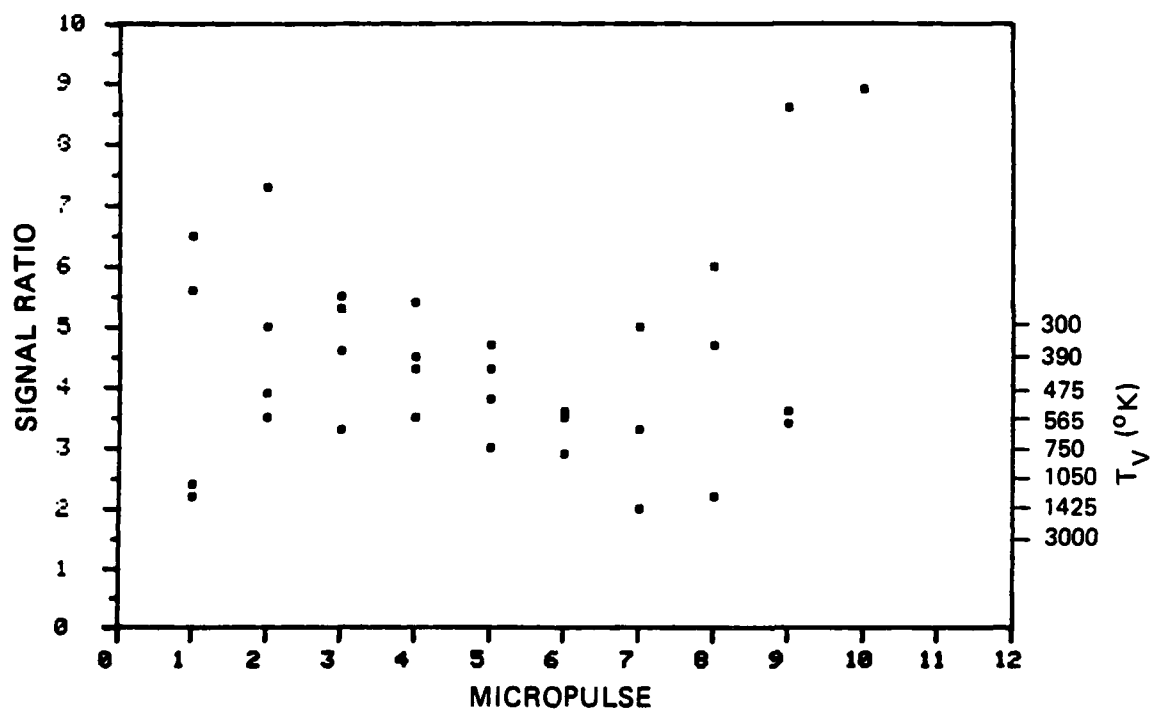
JA-2690-141

FIGURE 42 RATIOS OF 391.4-nm/423.6-nm SIGNALS VERSUS MICROPULSE
AT 100 torr



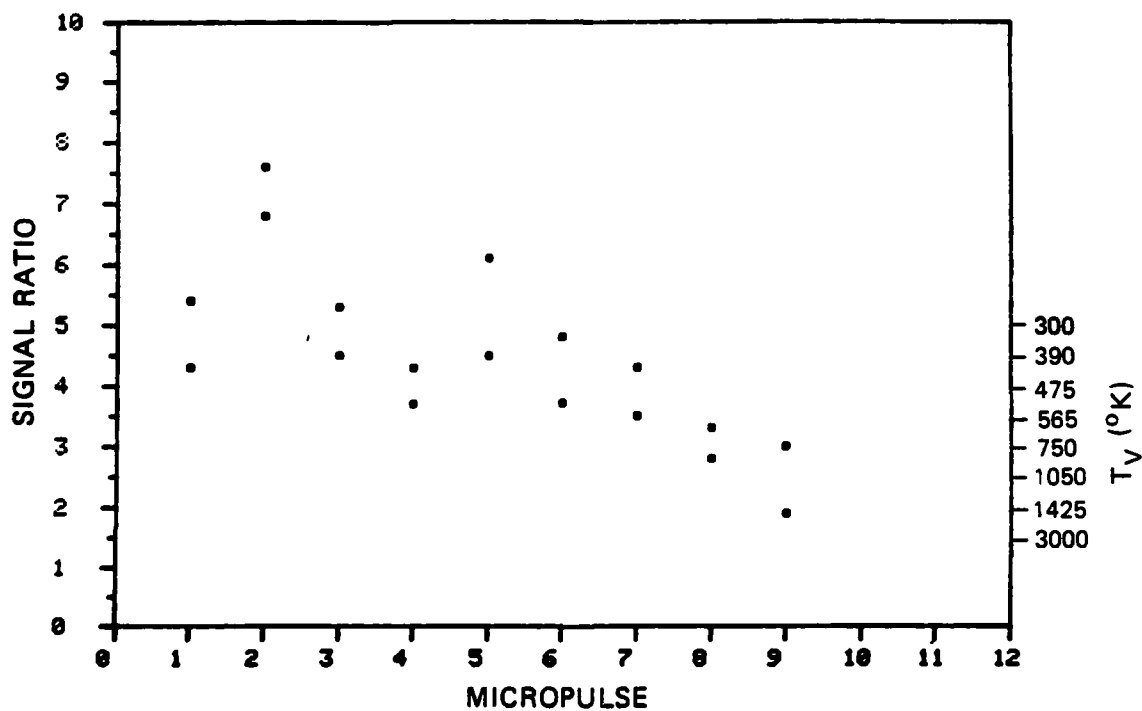
JA-2690-142

FIGURE 43 RATIOS OF 391.4-nm/423.6-nm SIGNALS VERSUS MICROPULSE
AT 50 torr



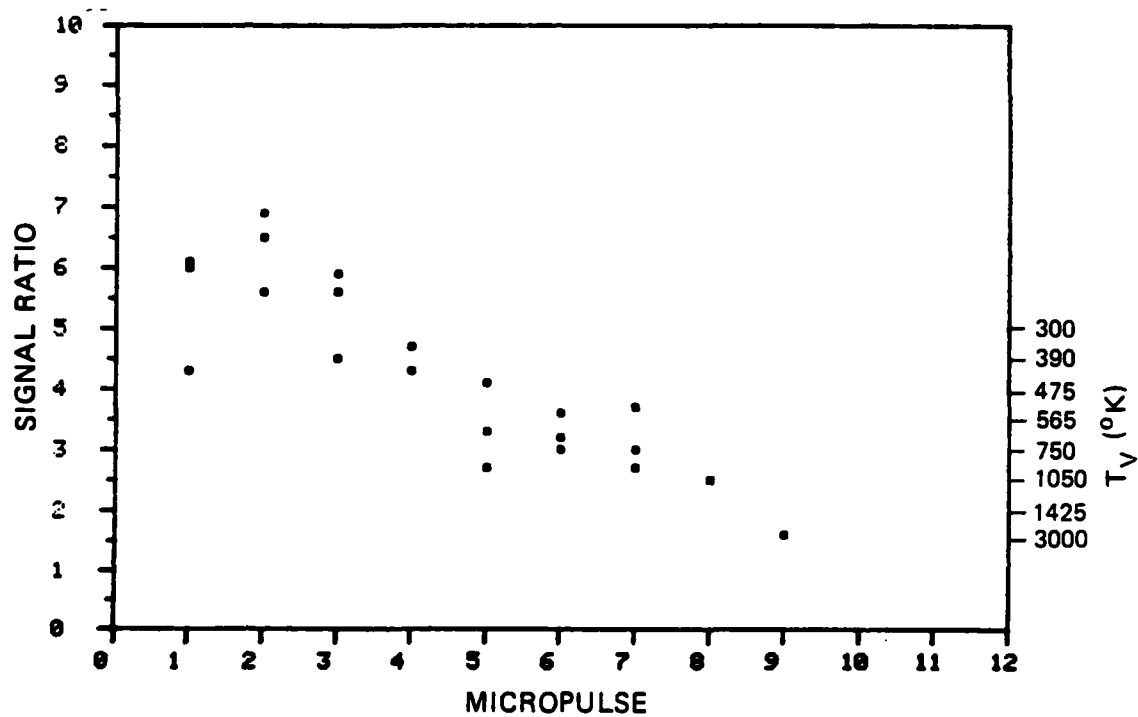
JA-2690-143

FIGURE 44 RATIOS OF 391.4-nm/423.6-nm SIGNALS VERSUS MICROPULSE
AT 30 torr



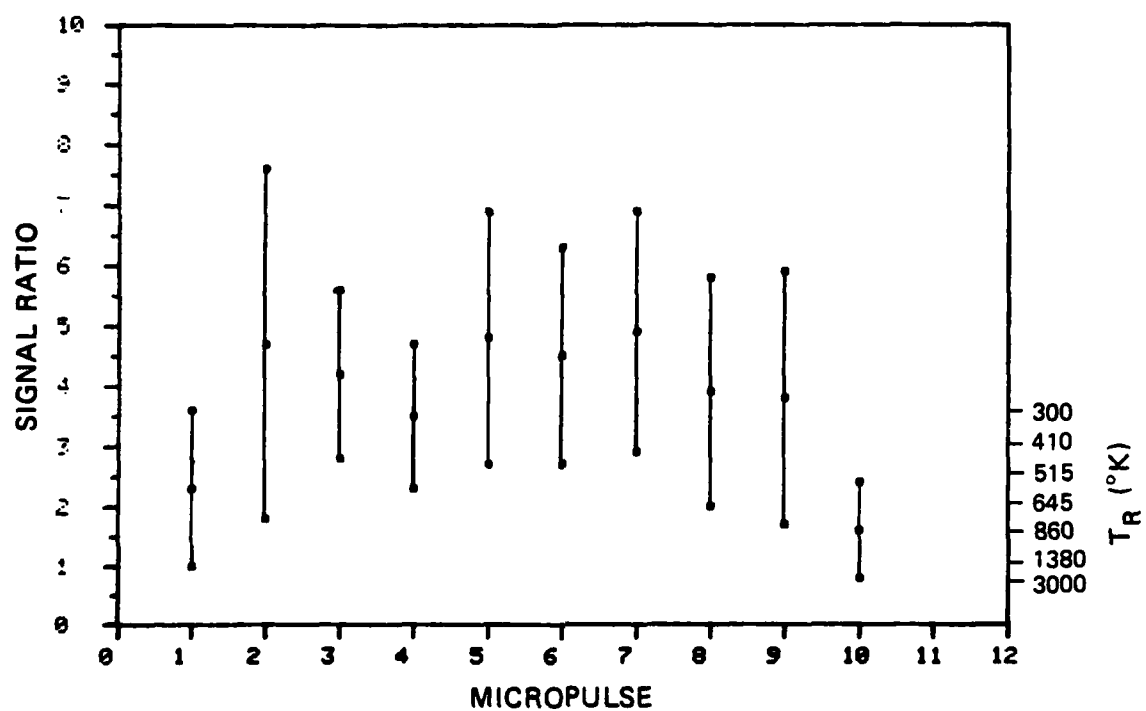
JA-2690-144

FIGURE 45 RATIOS OF 391.4-nm/423.6-nm SIGNALS VERSUS MICROPULSE
AT 10 torr



JA-2690-145

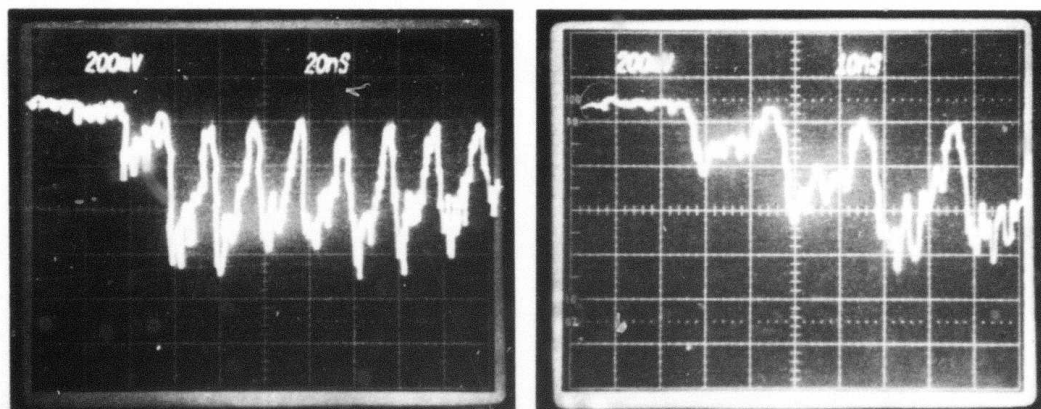
FIGURE 46 RATIOS OF 391.4-nm/423.6-nm SIGNALS VERSUS MICROPULSE
AT 5 torr



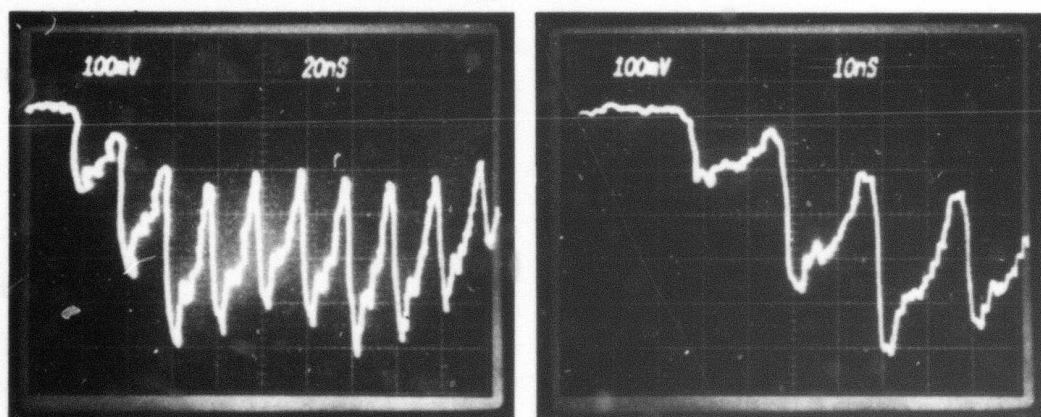
JA-2690-146

FIGURE 47 RATIOS OF 406.0-nm/403.0-nm SIGNALS VERSUS MICROPULSE
AT 580 torr (Mean and Standard Deviation)

391.4 nm



337.1 nm



JP-2690-86

FIGURE 48 FAR-FIELD INTENSITY HISTORIES FOR PHERMEX BEAM
PROPAGATING IN OPEN AIR
(Distance = 22 m, FOV \cong 7 m)